CHALMERS
UNIVERSITY OF TECHNOLOGY

Comparative study of the main electromagnetic models applied to melt pool prediction with gas metal arc: Effect on flow, ripples from drop impact, and

International Journal of Heat and Mass Transfer 194 (2022) 123068

Contents lists available at ScienceDirect

International Journal of Heat and Mass Transfer

journal homepage: www.elsevier.com/locate/hmt

Comparative study of the main electromagnetic models applied to melt pool prediction with gas metal arc: Effect on flow, ripples from drop impact, and geometry

P. Aryal [a], F. Sikström [a], H. Nilsson [b], I. Choquet [a,*]

[a] Department of Engineering Science, University West, Trollhättan 461 86, Sweden
[b] Department of Mechanics and Maritime Sciences, Chalmers University of Technology, Gothenburg 412 96, Sweden

ARTICLE INFO

Article history:
Received 30 January 2022
Revised 15 May 2022
Accepted 21 May 2022

Keywords:
Maxwell electromagnetic force model
Kou and Sun model
Tsao and Wu model
Metal transfer
Molten pool
Free surface oscillation
Gas metal arc

ABSTRACT

The present work concerns the electromagnetic force models in computational fluid dynamics simulations of melt pools produced with electric arcs. These are commonly applied to gas metal arcs with metal transfer, in welding and additive manufacturing. Metal drop impact on the melt pool is thus included in this study. The electromagnetic force models applied in literature use either numerical solutions of Poisson equations or one of the two analytical models developed by Kou and Sun, or Tsao and Wu. These models rely on assumptions for which the effect on the melt pool predictions remains to be understood. The present work thoroughly investigates those assumptions and their effects. It has been supported by dedicated experimental tests that did provide estimates of unknown model parameters and validation data. The obtained results show that the assumptions that fundamentally distinguish these three models change the electromagnetic force, including the relation between its components. These changes, which can also be spatially non-uniform, are large. As a result, these models lead to significantly different recirculation flow pattern, thermal convection, melt pool morphology, bead dimensions, and free surface response to the metal transfer. We conclude by proposing conditions in which each of these models is suited or questionable.

1. Introduction

Gas metal arc (GMA) is widely used in fusion welding with metal transfer because of its high deposition rate and ease of automation. It is also increasingly applied in additive manufacturing (direct energy deposition). The process of metal fusion with a GMA involves heat and mass transfer from an electrode wire through a thermal plasma arc, and coalescence of transferred metal drops with the melt pool. Although the arc and pool are interdependent [1], the unified modelling approach, which consists in computing coupled arc and melt pool models, is seldom used due to the complexity of the physics involved (see [2] and references therein). The decoupled approach, which benefits from a lower computational cost as underlined in [3], is instead more widely applied. This is also the approach used in this study, which focuses on the modelling of the melt pool. Then, the modelling of the effect of the arc on the metal alloy is simplified to source terms or boundary conditions, which need to be set to close the melt pool model. This especially involves determining the electromagnetic force.

Based on dimensional analysis, the main forces driving the fluid flow in GMA melt pools are known to be, in ascending order of importance, the viscous friction force, the buoyancy force, the capillary force and the thermocapillary (or Marangoni) force [4,5]. In comparison, the electromagnetic force is of the same order of magnitude as the thermocapillary force [5], or at a higher order [4], depending on the GMA process conditions. The momentum transferred by the droplets is also important to consider, as demonstrated by Na and Kim [6] and Murphy [7]. These authors used a computational model to compare melt pools predicted with and without the drop effect. In the early study by Na and Kim [6], the authors assumed a Gaussian distribution of the droplet velocity to model the momentum it transfers to the melt pool free surface. In the more recent study by Murphy [7], a self-consistent melt pool model was used, which includes the workpiece, as well the

* Corresponding author.
E-mail addresses: pradip.aryal@hv.se (P. Aryal), isabelle.choquet@hv.se (I. Choquet).

https://doi.org/10.1016/j.ijheatmasstransfer.2022.123068

Nomenclature

a_s	Activity of species s in solution [wt. %]
$\vec{A}$	Magnetic potential [T m^{-1}]
$\mathcal{A}$	Mushy zone permeability coefficient [-]
$\vec{B}$	Magnetic flux density (or magnetic field) [T]
c_p	Specific heat capacity at constant pressure [J kg^{-1} K^{-1}]
C_α	Interface compression factor (numerical) [-]
d	Gaussian distribution factor [-]
D	Diameter [m]
$\vec{E}$	Electric field [V m^{-1}]
f_{drop}	Frequency of drop transfer [s^{-1}]
f_l	Liquid fraction [-]
$\vec{F}$	Force applied (per unit volume) [N m^{-3}]
$\vec{F}_{\vec{J}\times\vec{B}}$	Electromagnetic force (per unit volume) [N m^{-3}]
$\vec{g}$	Gravitational acceleration [m s^{-2}]
h	Specific enthalpy [J kg^{-1}]
h_{sf}	Latent heat of fusion [J kg^{-1}]
h_{fv}	Latent heat of vaporization [J kg^{-1}]
I	Electric current [A]
$\boldsymbol{I}$	Identity tensor [-]
$\vec{J}$	Current density [A m^{-2}]
k	Thermal conductivity [W m^{-1} K^{-1}]
k_l	Constant related to the entropy of segregation [J kg^{-1} K^{-1}]
k_B	Boltzmann constant [J K^{-1}]
m	Atomic weight [kg atom^{-1}]
$\dot{m}$	Mass per unit time [kg s^{-1}]
$\vec{n}$	Unit vector locally normal to the free surface [-]
p	Pressure [Pa]
$\dot{q}$	Rate of heat transfer per unit area [W m^{-2}]
$\dot{Q}$	Rate of heat transfer per unit volume [W m^{-3}]
r	Radial distance [m]
(r, θ, z)	Cylindrical coordinates
R	Universal gas constant [J mol^{-1} K^{-1}]
R_w	Wire radius [m]
t	Time [s]
T	Temperature [K]
T_l	Liquidus temperature [K]
T_m	Melting temperature [K]
T_s	Solidus temperature [K]
T_v	Vaporization temperature [K]
$\vec{u}$	Fluid velocity [m s^{-1}]
$\vec{u}_r$	Interface compression velocity (numerical) [m s^{-1}]
$\vec{U}_{wf}$	Wire feed rate [m s^{-1}]
$\vec{U}_{wp}$	Workpiece travel velocity [m s^{-1}]
V	Electric potential [V]
(x, y, z)	Cartesian coordinates [m]
z	Vertical elevation [m]

Greek symbols

α	Volume fraction [-]
$\dot{\alpha}$	Volume fraction per unit time [s^{-1}]
β	Thermal expansion coefficient of liquid alloy [K^{-1}]
β_r	Retro-diffusion coefficient [-]
γ	Surface tension coefficient [N m^{-1}]
$(\gamma)_0$	Surface tension at T_m [N m^{-1}]
$\left(\frac{\partial\gamma}{\partial T}\right)_0$	Surface tension temperature gradient at T_m [N m^{-1} K^{-1}]
Γ_s	Surface excess at saturation [kg mol^{-1} m^{-2}]
ΔH^0	Standard heat of adsorption [J kg^{-1} mol^{-1}]
ϵ	Radiative emissivity [-]
ϵ_0	small constant [-]
η	Thermal efficiency [-]
θ	Polar angle [-]
κ	Free surface curvature [m^{-1}]
μ	Dynamic viscosity [Pa s]
μ_0	Permeability of free space [N A^{-2}]
ρ	Density [kg m^{-3}]
$\dot{\rho}$	Density per unit time [kg m^{-3} s^{-1}]
$\sigma_{arc,\vec{J}}$	Effective radius of the arc current density distribution [m]
$\sigma_{arc,p}$	Effective radius of the arc pressure distribution [m]
$\sigma_{arc,q}$	Effective radius of the arc heat flux distribution [m]
σ_e	Electrical conductivity [Ω^{-1} m^{-1}]
σ_{SB}	Stefan Boltzmann constant [W m^{-2} K^{-4}]

Subscripts

amb	Ambient condition
arc	Electric arc
conv	Convection
drop	Metal drop
l	Liquid state
m	Melting condition
pool	Melt pool
rad	Radiation
sat	Saturation
vap	Vaporization
s	Solid state
0	Arc centre location at the workpiece surface
1	Primary VOF-phase (metal alloy)
2	Secondary VOF-phase (shielding gas)

arc with the metal vapour and the electrode. The effects observed by these authors indicate that the force applied by the falling drop on the melt pool is of the same order of magnitude as the electromagnetic force. The electromagnetic force is thus among the leading order forces in GMA melt pools. However, the literature shows that there is not yet unanimity on how to model it when studying such melt pools with computational fluid dynamics.

Three different electromagnetic force models (EMF models) are being widely used in the literature. The first one is a numerical model that consists in solving partial differential equations governing the electromagnetic field. This model has two main variants. Both compute the electric potential and the current density in the same way. They differ through the computation of the magnetic field. In the first variant, which is the more general of the two, the magnetic vector field is derived from Ampère's law supplemented with Ohm's law, either directly or through the magnetic potential vector [8]. This variant is hereafter called the numerical EMF model. It is commonly applied when the arc and melt pool are simulated with a unified approach, as in [2]). However, it is less frequently used in the context of melt pools modelled with a decoupled approach. Nevertheless, Hashimoto et al. [9] used this numerical EMF model to supplement their decoupled melt pool model with drop detachment prediction. In the second variant, the Biot-Savart law is applied to compute the magnetic field [10]. A simplification is then made, which consists in assuming that the radial component of the current density has a negligible contribution to the magnetic field [11]. This EMF model was applied to GMA welding (GMAW) to understand the mechanisms leading to the formation of ripples on the melt pool and the re-solidified bead [12]. It was also used to study the effect on the melt pool of surface active elements at different concentrations in the wire and the workpiece [13], varied process parameters (e.g., current, volt-

age) [14], and operating the arc with and without pulsing of the electric current [15].

We also consider two analytical models which were introduced by Kou and Sun [16] in 1985, and by Tsao and Wu [17] in 1988. Their main advantage is to reduce the computational time through replacing partial differential equations by an integral function for the former and an algebraic expression for the latter. These analytical models were originally introduced for gas tungsten arc assuming a flat workpiece and an axisymmetric configuration. Several developments were made since then. For instance, the Kou and Sun model was adapted by Cho et al. [18] to a V-groove joint shape introducing coordinate mapping and an elliptically symmetric arc. Wu et al. [19] proposed coordinate rotation of the arc to adapt the Kou and Sun model to conditions where the arc axis is not orthogonal to the workpiece surface, as when welding horizontal fillet joints. Zhang and Wu [20] proposed an enhancement factor applied to each component of the Tsao and Wu EMF. More recently, Hamed Zargari et al. [21] who applied the Tsao and Wu model in double-ellipse mode to study tandem-pulsed GMA introduced a new factor in the vertical component of the EMF to increase the model accuracy. To study the effect of a V-groove angle in GMA welding, Chen et al. [22] extended the Tsao and Wu EMF model to V-groove joint shapes by using a body-fitted coordinate system. Ebrahimi et al. [23] applied a similar approach to investigate various groove shapes in GMA welding. The Tsao and Wu EMF model was also applied in additive manufacturing. For instance, Bai et al. [3] used it to analyse the thermal flow in multi-layer deposition with a plasma arc heat source.

The analytical EMF models seem to be the most commonly used today to study melt pools produced by an electric arc heat source with computational fluid dynamics. The model of Kou and Sun was applied to understand the effect of the melt flow on the formation of defects such as lack-of-fusion and porosity when welding narrow gap with a GMA linearly translated or moved following a circular motion trajectory (swing-arc) [24]. It was also used to study the effect of GMA process parameters (e.g., current, voltage) on the melt pool flow and geometry when the arc is electrically pulsed to transfer one drop metal per pulse [25], when the welding torch is tilted to investigate the forces driving the flow [26], or when the weld is covered with slag to study its interaction with the melt pool thermal flow [27]. It was also applied to understand how the convective pattern is modified when a GMA is supplemented with a second heat source operated in keyhole mode such as a laser beam [28] or a plasma arc [29]. The model of Tsao and Wu was as well highly employed to understand the melt pool thermal flow in GMAW and its effect on defect formation such as undercut and humping [30], and of the influence of various process conditions on the melt pool flow such as arc swing compared to no swing [31], and the presence of an additional heat source like a laser beam for hybrid welding of aluminium alloy [32], or a second GMA for tandem welding with steady or vibrated workpiece [33]. The EMF model of Tsao and Wu was also applied to analyse the thermal flow in wire-based direct energy deposition with plasma-arc [3] and with GMA [34].

To permit an analytic approximation of the electromagnetic field, simplifying assumptions were introduced by Kou and Sun [16] and by Tsao and Wu [17]. Simplifying assumptions are also used with the numerical EMF model applied to melt pool computational fluid dynamics simulations. The effect of these assumptions on the melt pool predictions is still poorly understood. Kumar and DebRoy [35] compared the components of the electromagnetic forces resulting from the Tsao and Wu and from the Kou and Sun models. However, to our knowledge, a comparative investigation of these electromagnetic force models, in particular with regards to their effect on the melt pool, has not yet been made. This is the subject matter of the present paper. The numerical and the two analytical electromagnetic force models, as well as the assumptions on which they are based, are first recalled in Section 2. Each of these force models was combined with a thermo-fluid model that is presented in Section 3. They were applied to simulate a GMA test case, which has also been conducted experimentally. This test case is introduced in Section 4. The computational results showing the effect of the modelling assumptions on the predicted melt pool are then compared and analysed.

2. Models for the electromagnetic force

The electric arc induces an electromagnetic force

$$\vec{F}_{\vec{J}\times\vec{B}} = \vec{J} \times \vec{B}, \tag{1}$$

that depends on the electric current density, $\vec{J}$ and the magnetic flux density $\vec{B}$ (simply called the magnetic field from now). The $\vec{J}$ and $\vec{B}$ fields should be determined in the melt pool and in the thermal plasma arc, at least to set the boundary conditions for the melt pool sub-region at the metal-arc interface. These vector fields obey the set of Maxwell equations supplemented by two closure relations, namely the equation governing charge conservation and the generalized Ohm's law. As this study is conducted with a fluid approach, the magnetohydrodynamics approximation can be made in both the melt pool and the thermal plasma arc (see e.g., [11] for more details) since the following assumptions are valid:

(i) The Debye length is much smaller than the characteristic length, so that there is local electro-neutrality.
(ii) The diffusion and thermodiffusion currents due to electrons are small compared to the drift current.
(iii) The characteristic time and length allow neglecting the displacement current compared to the current density (in Ampère' s law).
(iv) The Larmor frequency is much smaller than the average collision frequency of electrons, implying a negligible Hall current compared to the drift current.
(v) The magnetic Reynolds number is much smaller than unity, leading to a negligible induction current compared to the drift current.

Assumptions (i)–(v) imply that the electromagnetic phenomena are quasi-steady, the electric field $\vec{E}$ is irrotational, and the magnetic field has constant zero divergence. Therefore $\vec{E}$ and $\vec{B}$ can respectively be derived from a scalar electric potential V and a vector magnetic potential $\vec{A}$ that are uniquely defined imposing the Lorentz gauge (i.e., $\nabla\vec{A} = 0$). Then, the closed system of the Maxwell equations reduces to

$$\nabla \cdot (\sigma_e \ \nabla V) = 0, \tag{2}$$

$$\triangle\vec{A} = \mu_o \ \sigma_e \ \nabla V, \tag{3}$$

where the electric conductivity σ_e depends on e.g., the temperature. μ_o is the permeability of vacuum, and $\triangle$ denotes the Laplace operator. The current density and magnetic field are then derived from the solutions of these equations according to

$$\vec{J} = \sigma_e \ \vec{E} = -\sigma_e \ \nabla V, \tag{4}$$

$$\vec{B} = \nabla \times \vec{A}. \tag{5}$$

A difficulty is the coupling between the thermal plasma arc and the metal sub-regions. The coupling of these two sub-regions, which takes place through the sheath layers, is still an open problem when the interface region deforms in time and space as is the case at the melt pool free surface [36]. Additional simplifications are thus commonly introduced to circumvent this difficulty.

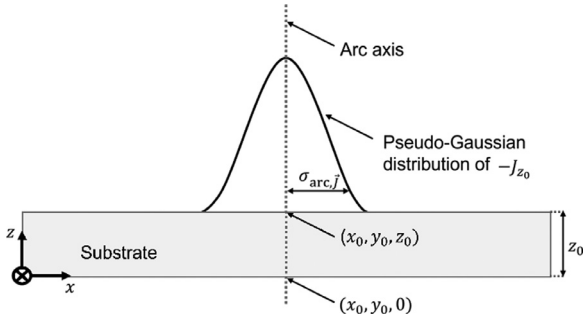

Fig. 1. Sketch of current density distribution on workpiece upper surface showing the convention used for axis orientation.

2.1. Numerical EMF model

To simplify the problem and evaluate the electromagnetic force in the melt pool without modelling the thermal plasma arc, it is also commonly assumed that

(vi) The electromagnetic part of the problem can be modelled as if the melt pool free surface was frozen (while the thermo-fluid model can predict free-surface deformation).

In addition, in this study

(vii) The current density distribution at the workpiece upper surface located at z_0, $\vec{J}(x, y, z_0) = \left(0, 0, J_{z_0}(x, y)\right)$, obeys a pseudo-Gaussian distribution such that

$$\left(\frac{\partial V}{\partial z}\right)_{z=z_0} = -\frac{Id}{\pi \sigma_e \sigma^2_{arc,\vec{J}}} \exp\left(\frac{-d\ r^2}{\sigma^2_{arc,\vec{J}}}\right) \quad \text{with} \quad r^2 = (x-x_0)^2 + (y-y_0)^2, \tag{6}$$

where z is along the electrode (and arc) axis direction shown in Fig. 1. I is the current, d the factor of the pseudo-Gaussian, $\sigma_{arc,\vec{J}}$ the effective radius of the arc with respect to the current density field, and x_0 and y_0 are the coordinates of the arc centre.

(viii) The electrical conductivity σ_e is constant.

Concerning assumption (vi), the surface is treated differently depending on the application. In electric arc welding the melt pool free surface is generally set flat (all the time along the simulated process) to compute the electromagnetic force. In direct energy deposition with a GMA, some authors set the contour of the frozen surface from scans of experimental beads [8]. The contour of the frozen surface can then be updated each time a new metal layer begins to be deposited. Assumption (vii) is valid if the surface is flat, but other current density distribution on flat surface could be used in Eq. (6), such as a double ellipsoid for instance. Besides, the restrictions (vii) and (viii) are not needed to proceed to a numerical solution of this EMF model. They are only required when looking for an analytic solution as in Sections 2.2 and 2.3. In the test cases of this study, the numerical EMF model uses a flat shape for the frozen surface of (vi) as well as the assumptions (vii)-(viii). This is for consistency purpose when comparing the different EMF models.

2.2. Kou and Sun EMF model

Kou and Sun [16] used a cylindrical coordinate system (r, θ, z) and supplemented (i)-(viii) with the following assumptions:

(ix) (a) The lower surface of the workpiece is electrically insulated, and
(b) the workpiece extends far away enough from the arc centre so that V can be set to zero on all the lateral boundaries of the workpiece (i.e. $r_{boundary} \to \infty$).

(x) The problem is axisymmetric, implying that the axial (B_z) and radial (B_r) components of the $\vec{B}$ field are everywhere equal to zero, as well as the azimuthal component, J_θ, of the current density field.

(xi) The azimuthal component, $B_\theta(r, z)$, of the magnetic field is defined from Ampère's law (formulated in integral form in [16]), given by

$$\frac{1}{r}\frac{\partial (r\ B_\theta(r,z))}{\partial r} = \mu_o\ J_z(r,z). \tag{7}$$

Note that, by construction, the EMF model of Kou and Sun satisfies the basic principle of current (or charge) conservation, and therefore assumption (ix) means that

(ix*) (a) The electric current cannot pass through the lower surface of the workpiece, so $J_z = 0$ at $z = 0$.
(b) The electric current passes through the lateral faces of the workpiece.

The constraint (ix*) is only a sub-part of (ix). Nevertheless, it might be problematic since experimental set-ups do not always permit to satisfy it. The workpiece is indeed often connected to the electrical ground through its lower surface lying on the welding table. Besides, it should be noticed that assumption (xi) is not contained in (x), and Eq. (7) is not based on axisymmetry alone. When using axisymmetry alone, as shown in [11], the complete expression of Ampère's law indeed involves a second contribution to B_θ through

$$\frac{\partial B_\theta(r,z)}{\partial z} = -\mu_o\ J_r(r,z). \tag{8}$$

If the problem is effectively axisymmetric and (ix) holds, the main difference between the numerical EMF model of Section 2.1 and the model of Kou and Sun therefore lies in neglecting the contribution of J_r to B_θ (assumption (xi)). Hence, if the above assumptions are valid, the simplified variant of the numerical EMF model with magnetic field defined from the Biot-Savart law (see Section 1) is equivalent to the model of Kou and Sun.

Assumptions (i)–(xi) allow deriving an analytic solution of Eqs. (2)-(3). The derivation steps were explained in detail by Kumar and DebRoy [35] and are not repeated here. With the convention of axis orientation and origin indicated in Fig. 1 they lead to

$$J_r = \frac{I}{2\pi}\int_0^\infty \lambda J_1(\lambda r)\ \exp\left(\frac{-\lambda^2\sigma^2_{arc,\vec{J}}}{4d}\right)\frac{\cosh[\lambda(z_0-z)]}{\sinh(\lambda z_0)}\ d\lambda, \tag{9}$$

$$J_z = -\frac{I}{2\pi}\int_0^\infty \lambda J_0(\lambda r)\ \exp\left(\frac{-\lambda^2\sigma^2_{arc,\vec{J}}}{4d}\right)\frac{\sinh[\lambda(z_0-z)]}{\sinh(\lambda z_0)}\ d\lambda, \tag{10}$$

$$B_\theta = -\frac{\mu_0 I}{2\pi}\int_0^\infty J_1(\lambda r)\ \exp\left(\frac{-\lambda^2\sigma^2_{arc,\vec{J}}}{4d}\right)\frac{\sinh[\lambda(z_0-z)]}{\sinh(\lambda z_0)}\ d\lambda, \tag{11}$$

where J_0 is the Bessel function of zero order and first kind, J_1 is the Bessel function of first order and first kind, and z_0 is the workpiece thickness (see Section 4.1, Table 1). The electromagnetic force field

in cartesian coordinates is then

$$(F_{\vec{j}\times\vec{B}})_x = -\frac{x-x_0}{r} J_z B_\theta, \tag{12}$$

$$(F_{\vec{j}\times\vec{B}})_y = -\frac{y-y_0}{r} J_z B_\theta, \tag{13}$$

$$(F_{\vec{j}\times\vec{B}})_z = J_r B_\theta. \tag{14}$$

2.3. Tsao and Wu EMF model

Tsao and Wu [17] also used the above assumptions (i)–(viii) and (x)–(xi) but not assumption (ix) to develop their EMF model. Instead they made the two following additional simplifications:

(xii) The radial component J_r of the current density in the workpiece is the average value through the workpiece thickness.
(xiii) The vertical component of the current density J_z and the angular component of the magnetic field B_θ decrease linearly with z down to zero at the lower surface of the workpiece (at $z = 0$).

It can be seen that, although (xii)–(xiii) and (ix*) are not equivalent, the assumptions (xii)–(xiii) satisfy the constraints listed in (ix*). It implies that (ix*) is common to the two analytical EMF models. The simplifications (xii)–(xiii) imply that the scalar Poisson equation governing the electric potential, Eq. (2), is no longer used. The simplified Eq. (7) governing the magnetic field is only solved at the workpiece upper surface and no longer within its volume. In this framework the electromagnetic force depends on $\vec{J}$ and $\vec{B}$ as already expressed in Eqs. (12)–(14), but the components of the current density and the magnetic field now write

$$J_r = \frac{I}{2\pi r z_0}\left[1 - \exp\left(\frac{-dr^2}{\sigma^2_{arc,\vec{J}}}\right)\right], \tag{15}$$

$$J_z = -\frac{Id}{\pi\sigma^2_{arc,\vec{J}}}\,\frac{z}{z_0}\,\exp\left(\frac{-dr^2}{\sigma^2_{arc,\vec{J}}}\right), \tag{16}$$

$$B_\theta = -\frac{\mu_0 I}{2\pi r}\,\frac{z}{z_0}\left[1 - \exp\left(\frac{-dr^2}{\sigma^2_{arc,\vec{J}}}\right)\right]. \tag{17}$$

3. Thermo-fluid model

Each of the above EMF models was combined with the thermo-fluid model described in this section to simulate the melt pool produced by a GMA. A one-fluid, unsteady and three-dimensional approach with free-surface capturing was used. It includes the shielding atmosphere and the metal in both solid and liquid states, with melting, re-solidification, and vaporization. The fluid flow equations were expressed in a fixed reference frame. In the model, the arc was at a fixed position and the workpiece was translated at the uniform velocity $\vec{U}_{wp} = -\vec{U}_{tr}$ (where U_{tr} is the travel speed) imposing appropriate boundary conditions on the velocity field. The thermal plasma arc and the metal transfer were simplified using closure models. The governing equations are first presented, followed by the closure models.

3.1. Governing equations

The fluids are treated as immiscible, mechanically incompressible and Newtonian. The flow is assumed to be laminar, so that no turbulence model is used. The deformation of the liquid metal free surface is tracked with a volume of fluid approach. The system of governing equations includes mass, momentum, and energy conservation, supplemented with a transport equation for the volume fraction of metal alloy. These equations respectively are

$$\partial_t \rho + \nabla\cdot(\rho\vec{u}) = \dot{\rho}_{drop}, \tag{18}$$

$$\begin{aligned}
&\partial_t\left(\rho\,\vec{u}\right) + \nabla\cdot\left(\rho\,\vec{u}\vec{u}\right)\\
&= -\nabla p + \nabla\cdot\left[\mu\left(\nabla\,\vec{u} + \left(\nabla\,\vec{u}\right)^T\right) - \frac{2}{3}\mu\left(\nabla\cdot\vec{u}\right)I\right] + \rho\,\vec{g}\\
&\quad - \rho_m\beta(T - T_m)\,\vec{g} - \mathcal{A}\frac{(1-f_l)^2}{f_l^3 + \epsilon_0}\left(\vec{u} - \vec{U}_{wp}\right)\\
&\quad + \left[\gamma\kappa\,\vec{n} + \frac{d\gamma}{dT}\left(\nabla T - \vec{n}\left(\vec{n}\cdot\nabla T\right)\right)\right]|\nabla\alpha|\,\frac{2\rho}{\rho_1+\rho_2}\\
&\quad + \vec{F}_{\vec{j}\times\vec{B}} + \vec{F}_{arc} + \vec{F}_{drop},
\end{aligned} \tag{19}$$

$$\begin{aligned}
&\partial_t(\rho c_p T) + \nabla\cdot(\rho c_p T\vec{u})\\
&= \nabla\cdot(k\nabla T) - h_{sf}\left[\partial_t(\rho f_l) + \nabla(\rho f_l\vec{u})\right]\\
&\quad - \left[\sum_i (h_{fv})_i(\dot{m}_{vap})_i + \epsilon\sigma_{SB}(T^4 - T^4_{amb})\right]|\nabla\alpha|\,\frac{2\rho}{\rho_1+\rho_2}\\
&\quad + \dot{q}_{arc} + \dot{q}_{drop},
\end{aligned} \tag{20}$$

$$\partial_t\alpha + \nabla\cdot(\alpha\vec{u}) + C_\alpha\nabla\cdot(\alpha(1-\alpha)\vec{u}_r) = \dot{\alpha}_{drop}, \tag{21}$$

where t denotes the time, $\vec{u}$ the velocity vector, p the pressure, T the temperature and α the volume fraction of metal alloy. In the metal $\alpha = 1$, in the atmosphere $\alpha = 0$, and at the interface region $0 < \alpha < 1$. The one-fluid density, ρ, dynamic viscosity, μ, specific heat capacity, c_p, and thermal conductivity, k, are defined by a mixture model based on the distribution of volume fraction according to

$$\phi = \alpha\phi_1 + (1-\alpha)\phi_2 \qquad \text{if} \quad \phi = \rho \text{ or } \mu, \tag{22}$$

$$\tilde{\phi} = \alpha\left[f_l\,\tilde{\phi}_{1,l} + (1-f_l)\tilde{\phi}_{1,s}\right] + (1-\alpha)\tilde{\phi}_2 \qquad \text{if} \quad \tilde{\phi} = k \text{ or } c_p. \tag{23}$$

Subscripts 1 and 2 refer to the primary VOF-phase (the metal alloy) and the secondary one (the shielding gas), respectively. Index s holds for the solid phase and l for the liquid one. The properties of the metal alloy and shielding gas are given in Section 4.2, Tables 2, 3 and 4, respectively. The mass fraction of liquid metal, f_l, ranges from zero in the solid region to one in the liquid region. It is defined by a continuous function with continuous derivative [37], given by

$$f_l = \frac{1}{2}\left(\text{erf}\left[\frac{4(T - T_m)}{T_l - T_s}\right] + 1\right), \tag{24}$$

where T_s is the solidus temperature, T_l is the liquidus temperature, and $T_m = 0.5(T_s + T_l)$ is the arithmetic averaged melting temperature.

Considering the right-hand side of these equations, in Eq. (18), the mass source term due to metal transfer in the form of drops is defined with the closure model of Section 3.2. In the momentum conservation equation, Eq. (19), the forces are, from left to right, the pressure force, the viscous friction force, the weight, the buoyancy force applied on the liquid alloy (Boussinesq approximation), the Darcy damping term active in the mushy zone, the capillary and the thermocapillary forces acting at the melt pool free surface, the electromagnetic force, the arc pressure force, $\vec{F}_{arc}$, and the

force caused by the momentum of the injected drops, $\vec{F}_{drop}$. The two last forces are defined in Section 3.2. For the electromagnetic force, $\vec{F}_{\vec{j}\times\vec{B}}$, three alternatives are treated using the three EMF models of Section 2. The other forces are defined here. In the viscous friction force, $\boldsymbol{I}$ denotes the identity tensor. Next, $\vec{g}$ is the gravitational acceleration, β the thermal expansion coefficient of the liquid alloy, ρ_m the alloy density at the melting temperature T_m. $\mathcal{A}$ is the permeability coefficient and $\epsilon_0 = 10^{-3}$ (dimensionless) is a small constant to prevent from division by zero. The Peclet number adjacent to the solid-liquid interface calculated as introduced by Ebrahimi et al. [38], leads to $\mathrm{Pe}^\star = 2$ for the GMAW test case of this study. It was shown in [38] that at this order, $\mathrm{Pe}^\star = \mathcal{O}(1)$, the numerical results have only a low sensitivity to the value of $\mathcal{A}$. Besides, a too large $\mathcal{A}$-value may lead to numerical oscillations, the recommended upper-bound being 10^7. In this work $\mathcal{A}$ was set to 10^6 (dimensionless).

The surface tension coefficient, γ, is a function of both the temperature and the fraction of surfactant present in the alloy, according to [39]

$$\gamma = \gamma_0 + \left(\frac{\partial\gamma}{\partial T}\right)_0 (T - T_m) - RT\Gamma_s \ln[1 + k_l a_s \exp(-\Delta H^0/RT)], \tag{25}$$

where γ_0 and $\left(\partial\gamma/\partial T\right)_0$ are the surface tension and the surface tension temperature gradient of the dominant metal alloy element (here Fe) at temperature T_m. The last term at the right-hand side of the Eq. (25) is the influence of the alloying element. R is the universal gas constant, Γ_s the surface excess at saturation, k_l a constant related to the entropy of segregation, a_s the weight percentage of surface active element, and ΔH^0 the standard heat of adsorption. The free surface curvature, κ, and the unit vector locally normal to the free surface, $\vec{n}$, are given by

$$\kappa = -(\nabla \cdot \vec{n}), \quad \text{and} \quad \vec{n} = \frac{\nabla\alpha}{|\nabla\alpha|}. \tag{26}$$

As the density of the atmosphere and liquid alloy differ by several orders of magnitudes, the last factor in the capillary and thermocapillary forces is introduced so that surface tension acceleration remains independent of density [40].

In the energy conservation equation, Eq. (20), h_{sf} is the latent heat of fusion and h_{fv} the latent heat of vaporisation. The second term at the right-hand side is related to melting and resolidification of the alloy. It includes a convective contribution as phase change in an alloy is non-isothermal. The third term describes vaporisation of alloy constituents. It is modelled for the two major constituents alone assuming that they have a uniform %wt in the alloy, as element diffusion is neglected. Condensation is ignored. The mass flux of evaporation of an element is given by (see e.g. [41])

$$\dot{m}_{vap} = p_{sat}\sqrt{\frac{m}{2\pi k_B T}}(1 - \beta_r), \tag{27}$$

where m is the element atomic weight, and k_B the Boltzmann constant. In the alloy, the mass flux $\dot{m}_{vap}$ of a constituent i is weighted by its mass fraction, leading to the term $(\dot{m}_{vap})_i$ in Eq. (20). The retro-diffusion coefficient, β_r, is assumed to be zero. The saturated vapor pressure of the constituent writes

$$p_{sat} = p_{amb}\,\exp\left[\frac{m h_{fv}}{k_B T_v}\left(1 - \frac{T_v}{T}\right)\right], \tag{28}$$

where p_{amb} is the ambient pressure at standard condition (=101325 Pa), and T_v the vaporisation temperature at standard condition. The third term at the right-hand side of Eq. (20) is the radiative cooling at the metal surface according to the grey body model. ϵ_{rad} is the radiative emissivity of the metal, and σ_{SB} the Stefan-Boltzmann constant. The energy source term due to the electric arc, $\dot{q}_{arc}$, and the transferred metal drops, $\dot{q}_{drop}$, are defined by closure relations presented in Section 3.2.

The transport Eq. (21) is a modified VOF formulation introduced by Weller [42]. The third term of Eq. (21), which is only active at the interface, aims at enhancing the interface sharpening by reducing the numerical smearing of α. $\vec{u}_r$ is the compression velocity and C_α the compression factor [42]. In this study C_α is set to 1 to satisfy conservation. The source term $\dot{\alpha}_{drop}$ due to metal transfer is defined in Section 3.2.

3.2. Arc and metal transfer closure source terms

As electrode melting and thermal plasma arc are not predicted by the model, their effect on the melt pool is included through closure relations. The periodic metal transfer from the electrode is modelled injecting in the computational domain drops of molten alloy that are initially assumed to be identical, uniform, and spherical. At injection the diameter of a drop is defined according to (see e.g., [27])

$$D_{drop} = \left(6R_w^2\frac{U_{wf}}{f_{drop}}\right)^{1/3}, \tag{29}$$

where R_w is the wire radius, U_{wf} is the wire feed rate, and f_{drop} the frequency of the drop transfer. The drop velocity, $\vec{u}_{drop}$, temperature, T_{drop}, and centre location $(x_{drop}, y_{drop}, z_{drop})$ at injection are set based on experimental observation. At these conditions drop injection creates locally a periodic source term of mass $\dot{\rho}_{drop} = f_{drop}\rho_1$, momentum $\vec{F}_{drop} = \dot{\rho}_{drop}\vec{u}_{drop}$, thermal energy $\dot{q}_{drop} = \dot{q}_{arc\to drop}$, and metal volume fraction $\dot{\alpha}_{drop} = f_{drop}\alpha_{drop}$.

The electric arc acts on the melt pool through pressure and drag force, as well as heat transfer that is mainly due to temperature gradient and free electron enthalpy. In studies opting for a decoupled approach, the heat transfer from the arc is described as an overall phenomenon without distinguishing the different types of contributions. The drag force applied by the arc on the melt pool surface is often omitted, as in [12,14,25,26,32–34] concerning the examples discussed in Section 1. This is also the approach used in this study.

The arc pressure force is applied at the free surface. It is therefore modelled in a similar way as the surface tension force (see Section 3.1), as

$$\vec{F}_{arc} = p_{arc}\,|\nabla\alpha|\,\frac{2\rho}{\rho_1 + \rho_2}, \tag{30}$$

where p_{arc} is the pressure exerted by the arc. It is calculated using the empirical relation proposed by Lin and Eagar [43] given by

$$p_{arc} = \frac{\mu_0 I^2}{4\pi^2\sigma_{arc,p}^2}exp\left(-\frac{r^2}{2\sigma_{arc,p}^2}\right), \tag{31}$$

where $\sigma_{arc,p}$ is the arc pressure distribution parameter.

The rate of heat input from the arc per unit area of the workpiece surface is assumed to obey a Gaussian distribution as in several previous studies e.g., [12,25]. This choice is supported by the side view images of the arc, which were acquired during the experiments (see Section 4.1). It is thus expressed as

$$\dot{q}_{arc} = \frac{\eta_{arc\to pool} VI}{2\pi\sigma_{arc,q}^2}\exp\left(-\frac{r^2}{2\sigma_{arc,q}^2}\right), \tag{32}$$

where $\sigma_{arc,q}$ is the arc heat flux distribution parameter, and $\eta_{arc\to pool}$ the fraction of the process electric power that is transferred from the arc to the melt pool. It is defined from the arc thermal efficiency,

$$\eta_{arc} = \eta_{arc\to pool} + \eta_{arc\to drop}, \tag{33}$$

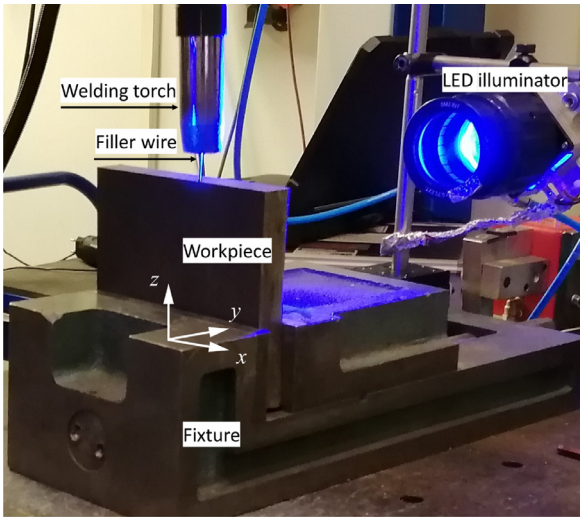

Fig. 2. Picture of the welding set-up.

and requires determining the fraction of the process electric power transferred from the arc to permit metal transfer

$$\eta_{arc\to drop} = \frac{\dot{Q}_{arc\to drop}}{VI}. \tag{34}$$

The rate of heat transferred from the arc to the metal wire to form drops includes solid metal heating, fusion, and liquid metal heating up to T_{drop} according to

$$\dot{Q}_{arc\to drop} = \frac{\pi D_{drop}^3}{6} f_{drop} \times\left[\rho_{1,s}(c_p)_{1,s}(T_s - T_{amb}) + \frac{\rho_{1,s}+\rho_{1,l}}{2} h_{sf} + \rho_{1,l}(c_p)_{1,l}(T_{drop} - T_l)\right]. \tag{35}$$

To complete the above closure relations and Eq. (6), the parameters η_{arc}, d, $\sigma_{arc,q}$, $\sigma_{arc,j}$, $\sigma_{arc,p}$, and T_{drop} were estimated for the test case of this study, as reported in Section 4.2.

4. Test case

The GMA test case of this study was investigated both experimentally and numerically. The experiments were conducted to collect data that permit closing the model and to provide validation data. The experimental set-up is therefore presented first, in Section 4.1. Then, the parameters entering the source terms and boundary conditions for the arc and drop are specified in Section 4.2, as well as the material data. Next, the computational domain as well as boundary and initial conditions are presented in Section 4.3. Finally, the main characteristics of the solution method are given in Section 4.4.

4.1. Experimental set-up for data collection

Bead-on-plate GMAW experiments were carried out in pulsed mode with one drop of metal transferred per pulse. Figure 2 shows a picture of the experimental set-up. It consisted of a power source, an ABB robot, a wire feeding system, a gas shielding system, and a computer controlled measurements system. The workpiece with dimensions 150 mm × 20 mm × 60 mm (length × width × thickness) and the 1.2 mm diameter filler wire were both made of Invar 36, although some of the minor elements differed slightly. The lower third of the workpiece was clamped in a fixture connected to the ground. The welding torch was maintained perpendicular to the workpiece and the contact-tip-to-workpiece distance was 16 mm.

Table 1
Parameters used in both experiments and simulations made with Invar 36 workpiece and filler wire.

Parameter	Notation	Value	Unit
Workpiece thickness	z_0	60	mm
Welding current (average)	I	225	A
Arc voltage (average)	V	25.6	V
Pulse frequency	f_{drop}	156	Hz
Filler wire radius	R_w	0.6	mm
Wire feed rate	U_{wf}	8	m min^{-1}
Welding travel speed	U_{tr}	8	mm s^{-1}

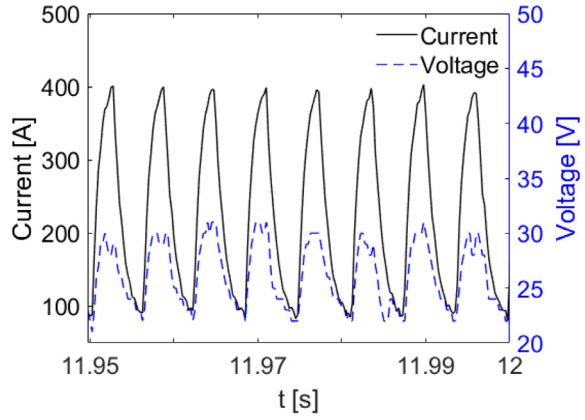

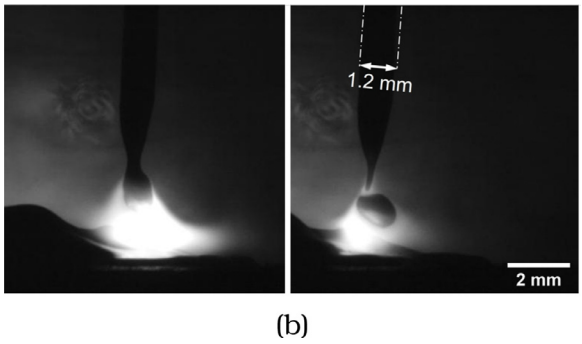

Fig. 3. (a) Sample of the electrical signal waveform recorded during the experiments. (b) Side view images of the one pulse one drop GMAW before and after drop detachment.

Pure argon gas was flowing through the welding torch at a constant flow rate of 15 l/min to shield the molten metal from the atmosphere. A single bead was deposited along the centreline of the workpiece using the process parameters reported in Table 1. This operation was repeated three times. The electrical signals were recorded using a computer data acquisition system at a sampling frequency of 4kHz. Figure 3a shows a sample of their waveforms. The value of the electric current and arc voltage ranged approximately from 90 to 400 A and 22 to 30 V, respectively. These time-variations are not considered in the simulations.

High speed imaging with an acquisition rate at 10,000 frames per second was used to capture drop size and motion, specifically drop velocity towards impingement into the melt pool. A collimated high power LED emitting 10 W optical power at a center wavelength of 450 nm was positioned on one side of the workpiece to provide backlighting during imaging. On the other side, a camera (IDT CCM-1540) was positioned to capture side view im-

ages of the process interaction zone. A dielectric-coated spectral filter with a center wavelength of 450 nm and a full width half max of 40 nm was mounted in the optical path of the camera matching the spectral distribution of the LED output power. The setup, shown in Fig. 2, was optimized to make the metal transfer visible through the arc attenuating partially the light entering the camera. However, the arc could still be distinguished in most of the captured images. An example of images can be seen in Fig. 3b. The captured images were used to extract data for the effective radius of the arc, drop size, and impingement drop speed. Besides, cross-sections of the weld beads were made at 55 mm, 65 mm and 75 mm from the start of the weld. The sectioned specimens were mounted in epoxy resin, polished and etched using Marble's reagent. The samples subjected to this standard metallographic procedure were then analysed in a light optical microscope.

4.2. Closure parameters and material data

The closure parameters for arc and metal drop modelling were collected from the literature and the experiments of Section 4.1. The total arc efficiency was set to $\eta_{arc} = 0.85$, based on a trial-and-error approach applied to reproduce numerically the dimensions of the bead cross sections obtained in the experiments. This value is at the high end of the range experimentally evaluated for GMAW (from about 0.68 to 0.85, see [44] and references therein). The pseudo-Gaussian distribution factor was set to the standard value $d = 3$, as proposed by e.g., Kou and Sun [16]. The arc heat flux distribution parameter, $\sigma_{arc,q}$, is known to be governed by several process parameters including the arc current and the arc length, as shown in e.g., [45] within the frame of gas tungsten arcs (GTA). Compared to GTA, a difficulty appears when the electrode is non-refractory, or when the elevation of the melt pool free surface varies with time as the arc length then changes with time. When modelling the melt pool with a decoupled approach, this variation with time uses to be neglected. The distribution parameter $\sigma_{arc,q}$ can then be approximated from spectral analysis or from measured irradiation using Abel inversion [46]. In the absence of such means, it is also commonly approximated either from arc simulation, or from empirical equations derived for gas tungsten arc welding, or from images of the thermal plasma arc. For instance, Wu et al. [47] did simulate a plasma arc assuming a flat workpiece surface to determine $\sigma_{arc,q}$, and then used this parameter to model a melt pool with keyhole. Ebrahimi et al. [48] applied a fitted function of the arc length and arc current based on experimental measurements made by Eagar and Tsai [45] for GTA on water cooled workpiece. Estimation from images was used in this study by manually defining a reasonable pixel intensity threshold to define the arc distribution and then measure the diameter at a reference level in z-direction using imageJ tool software as described by Zhu et al. [49]. A set of such images can be seen in the supplementary material, S1. Measurements from captured arc images for two complete pulsation cycles (120 images) were used and the average value of the diameters resulted in $\sigma_{arc,q} = 1.4$ mm as estimate. The arc pressure was assumed to have the same distribution as the arc heat flux. The current distribution parameter was adjusted by trial-and-error to $\sigma_{arc,j} = 1$ mm to reproduce the penetration depth obtained experimentally from the macrograph images. The adjustment was performed using the most general of the three EMF models, that is the numerical model of Section 2.1.

Concerning drop conditions at detachment from the electrode wire, the vertical position z_{drop} was estimated to 2.1 mm above the workpiece upper surface from the high-speed camera observation. The frequency of the drop transfer was obtained from the welding data logger. In the studied process, the metal drops impact the melt pool with a high velocity. The drop speed was estimated before the impact from the high-speed images leading to 1.3 m s^{-1}.

Table 2
Material properties of Invar 36 (used for both workpiece and metal drops).

Property	Value	Unit
$\rho_{1,s}$	8130 [53]	kg m^{-3}
$\rho_{1,l}$	7275 [54]	kg m^{-3}
T_s	1702 [53]	K
T_l	1723 [53]	K
μ_1	$10^{-0.619+2334T^{-1}} \times 10^{-3}$ [55]	kg m^{-1} s^{-1}
$(c_p)_{1,s}$	398 + 0.19 T [56]	J kg^{-1} K^{-1}
$(c_p)_{1,l}$	801 [54]	J kg^{-1} K^{-1}
$k_{1,s}$	6.293 + 0.01185 T [56]	W m^{-1} K^{-1}
$k_{1,l}$	2.755 + 0.01264 T [54]	W m^{-1} K^{-1}
γ_0	1.92 [57]	N m^{-1}
$\left(\frac{\partial\gamma}{\partial T}\right)_0$	- 3.97$\times$ 10^{-4} [57]	N m^{-1} K^{-1}
Γ_s	1.3 $\times$ 10^{-8} [39]	kg mol^{-1} m^{-2}
k_l	0.00318 [39]	-
a_s	0.004	wt. %
ΔH^0	-1.66 $\times$ 10^8 [39]	J kg^{-1} mol^{-1}
h_{sf}	2.76 $\times$ 10^5 [54]	J kg^{-1}
β	(12.357 + 0.001536 T) $\times$ 10^{-6} [56]	K^{-1}
ϵ_{rad}	0.7 [52]	-

Table 3
Vaporisation properties of the two main metal constituents [58].

Constituent	Property	Value	Unit
Fe (64%wt):	m	9.273280 $\times$ 10^{-26}	kg atom^{-1}
	T_v	3135	K
	h_{fv}	6.260 $\times$ 10^6	J kg^{-1}
Ni (36%wt):	m	9.746268 $\times$ 10^{-26}	kg atom^{-1}
	T_v	3186	K
	h_{fv}	6.787 $\times$ 10^6	J kg^{-1}

This value is also in good agreement with the experimental results of Lin et al. [50] for GMAW with 1.2 mm wire. To maintain consistency, all the model parameters were kept the same in all the simulated cases.

The material properties used in the simulations are reported in Tables 2–4. Constant values were assumed for the argon gas properties. The cases computed resulted in a maximum temperature less than 3000 K. The thermal conductivity and specific heat capacity of argon show insignificant variations with T when 300 $\leq$ T $\leq$ 3000 K [51]. However, in this temperature range the argon density decreases with T while its viscosity increases T [51]. Nevertheless, in the arc area the effect of these variations is negligible compared to the intensity of the arc source terms. Outside the arc area, the effect of this simplification on the computed alloy fields remains to be evaluated. During the experiments, a thin oxide layer was observed floating on the melt pool free surface. The radiative emissivity was thus set based on the experimental measurements of Barka et al. [52] for Invar 36 at high temperature in the presence of a thin oxide layer.

4.3. Computational domain, boundary and initial conditions

A 10 mm wide cuboid domain corresponding to half of the workpiece along the y-direction (see Fig. 2) was used for all the

Table 4
Material properties of argon gas at 300 K, [59].

Property	Value	Unit
ρ_2	1.6337	kg m^{-3}
μ_2	2.26 $\times$ 10^{-5}	kg m^{-1}s^{-1}
$c_{p,2}$	520	J kg^{-1} K^{-1}
k_2	0.08	W m^{-1} K^{-1}

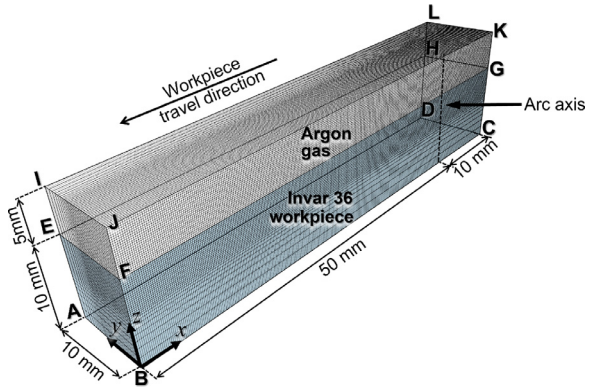

Fig. 4. Computational domain with metal and argon at the initial time.

simulations. This is equivalent to assuming symmetry although flow instability might occur in the melt pool due to e.g., the Marangoni recirculation induced by the presence of surfactant [60]. A symmetry boundary condition was thus applied to all the variables at $y = 0$, which coincides with the face BCGF in the computational domain of Fig. 4. Dimensions and conditions along the other directions were model dependent, and will be described later. In all the computations of this study the corner B (see Fig. 4) defines the origin of the domain.

Concerning the numerical EMF model, the computational domain used to solve Eqs. (2)-(3) includes only the metal subdomain of Fig. 4 since the atmosphere does not need to be considered at this stage. It was designed long enough along the travel direction to contain the domain needed for the thermo-fluid model. In a preliminary study, the influence of the thickness and length of the simulated workpiece on the EMF-fields was investigated. It was concluded that it is important that the electromagnetic boundary conditions can satisfy symmetry to comply with the modelling assumption (x) made by the analytical EMF models. The domain length along x was thus set identical on both sides of the arc. The arc axis was positioned at the centre ($x_0 = 50$ mm) of a domain that spanned 100 mm in the x-direction. The current density distribution defined in Eq. (6) was applied as boundary condition for the electric potential, Eq. (2), at the upper surface of the workpiece (EFGH at z_0) with the parameters specified in Section 4.2. To investigate the solution (in)dependence with respect to the position of the lower boundary surface (ABCD in $z = 0$), domains of various thicknesses were used. Two cases are reported below with $z_0 = 4$ mm and $z_0 = 10$ mm. Similar solutions were obtained with the experimental configuration and with a 10 mm thick workpiece whose lower face was set to V=0 while the lateral faces were electrically insulated. Results obtained with lateral grounding are also discussed later. The boundary conditions for the magnetic potential, Eq. (3), were set to zero gradient at z_0 and $z = 0$, and to zero on all the other metal boundaries.

The computational domain used to solve the thermo-fluid model, Eqs. (18)-(21), is shown in Fig. 4. It spans 60 × 10 × 15 mm in the x, y, and z directions, respectively. Its lower part was initialized with a 10 mm thick solid workpiece at 300 K and $\alpha = 1$, and the upper part with a 5 mm thick layer of argon gas at rest, at atmospheric pressure, 300 K, and $\alpha = 0$. The boundary conditions applied to Eqs. (18)-(21) are summarized in Table 5.

In Table 5, the rate of heat transfer by convection is $\dot{q}_{conv} = h_{conv}(T - T_{amb})$ with the constant $h_{conv} = 100$ W m^{-2} K^{-1} [8,61]. The ambient conditions are $T_{amb} = 300$ K, and $P_{atm} = 101325$ Pa. At the workpiece boundaries AEFB, ABCD, and EIJF the temperature gradient was extrapolated along the direction normal to the boundary.

Table 5
Boundary conditions for the thermo-fluid model.

Boundary	Variable			
	$\vec{u}$	p	T	α
AEFB	$\vec{u} = \vec{U}_{wp}$	$\partial_x p = 0$	$-k\partial_x T = \text{const}^a$	1
AEHD	$\partial_y u_y = 0$	$\partial_y p = 0$	$-k\partial_y T = \dot{q}_{conv}$	1
HGCD	$\vec{u} = \vec{U}_{wp}$	$\partial_x p = 0$	$T = T_{amb}$	1
ABCD	$\partial_z u_z = 0$	$\partial_z p = 0$	$-k\partial_z T = \text{const}^a$	1
BFGC	$\partial_y u_y = 0$	$\partial_y p = 0$	$\partial_y T = 0$	$\partial_y \alpha = 0$
EIJF	$\partial_x u_x = 0$	$p = p_{atm}$	$-k\partial_x T = \text{const}^a$	$\partial_x \alpha = 0$
EILH	$\partial_y u_y = 0$	$p = p_{atm}$	$-k\partial_y T = \dot{q}_{conv}$	0
LKGH	$\partial_x u_x = 0$	$p = p_{atm}$	$-k\partial_z T = \dot{q}_{conv}$	0
JKGF	$\partial_y u_y = 0$	$\partial_y p = 0$	$\partial_y T = 0$	$\partial_y \alpha = 0$
ILKJ	$\partial_z u_z = 0$	$p = p_{atm}$	$-k\partial_z T = \dot{q}_{conv}$	0

[a] The gradient is extrapolated.

At injection, the drop center was aligned with the arc axis thus $x_{drop} = x_0 = 50$ mm, and $y_{drop} = y_0 = 0$ mm. The vertical position z_{drop} was obtained from experimental observation (see Section 4.2). The fluid velocity ($\vec{u}_{drop}$ = (0; 0; -1.3) m s^{-1}) and temperature ($T_{drop} = 2100$ K) were assumed uniform throughout the drop. Contrary to $\vec{u}_{drop}$, T_{drop} could not be measured in the experiments of this study. It was therefore set from a GMA study by Zhou et al. [8], which was selected because of its similar range of process conditions. To initialize the drops, the quantity α_{drop} was set at each injection patching on the computational mesh a sphere of diameter D_{drop} centred in $(x_{drop}, y_{drop}, z_{drop})$.

As the numerical EMF model was solved using a large domain, the computed electromagnetic force fields were mapped cell to cell about the centre of the arc to the smaller thermo-fluid domain shown in Fig. 4. These mapped fields were used as body force source term in the momentum equation. It was ensured that the electromagnetic force fields in the vicinity of the arc axis remained identical before and after mapping.

4.4. Solution method

The EMF and thermo-fluid models were implemented in the OpenFOAM open-source software. The numerical EMF model was solved prior to the thermo-fluid model, setting the final convergence criteria to 10^{-8} for both $\vec{A}$ and V. Concerning the thermo-fluid model, the pressure-velocity coupling was solved using the Pressure-Implicit with Splitting of Operators (PISO) algorithm. The discretization of the convective term in the VOF equation was achieved by the Van Leer scheme, which is a second-order scheme that ensures boundedness of the scalar field α between 0 and 1. The Limited Linear scheme was used for the remaining convective terms in the governing equations. The Limited Linear scheme is a blended 1st/2nd order scheme that returns a first-order upwind differencing scheme in regions with a rapidly changing gradient and the second-order central differencing scheme elsewhere. The diffusion term in the governing equations was discretized using the central differencing scheme. The highly coupled governing equations were solved iteratively for each time step until the predefined criteria for convergence were satisfied before advancing to the next time step. The convergence criteria on the residual value was set to 10^{-12} for volume fraction, 10^{-8} for pressure and velocity, and 10^{-10} for temperature. The time stepping for advancing the solution was adjusted automatically imposing a maximum Courant number of 0.1 and a maximum allowed time step of 10^{-5} s.

A first grid study was conducted with the EMF model, and a second with the thermo-fluid model, using in each study 4, 5 and 6 cells per millimetre. When performing the second grid study with the thermo-fluid model, the coarse, medium and fine mesh had 375 360, 660 000 and 2 054 250 cells, respectively. It led to a fully developed melt pool with variation in penetration depth,

half-width and length below 6% for the medium compared to the coarse mesh, and 1% for the fine compared to the medium mesh. The medium-sized mesh provided a good compromise between quality of the solution and computational time. The mesh used for all the calculations presented hereafter thus has a uniform grid size of 0.2 mm in x, $0 \geq y \geq 6$ mm, and $0 \geq z - z_0 \geq$ -6 mm to ensure that the electromagnetic force variations are captured and that the melt pool is within the region of uniform cell size. Outside that region a cell to cell expansion ratio of 1.14 was applied. Besides, this mesh implies that 6 cells are used to discretize the droplet along its diameter, which is more than the minimum of 4 mesh cells usually recommended, as in [27] and references therein. Each simulation was executed in parallel using 20 cores Intel Xeon Gold 6130 CPU @ 2.90 GHz $\times$ 32 on a computing cluster provided by the Swedish National Infrastructure for Computing (SNIC). The computational time per simulation with the thermo-fluid model and the medium-sized mesh took about 168 h of physical time ($\approx$ 3360 Core hours) to simulate 12 s of GMAW.

5. Results and discussion

Experimental set-ups do not always comply with assumption (ix*). For instance, the electric potential (V) is often grounded under the workpiece through the working table, or as in this study through a fixture that covers only the lower part of lateral faces of the workpiece. Besides, it can be seen in the literature that the analytical EMF models were applied to a variety of workpiece thicknesses ranging from thin (e.g., 2.3 mm [62], 4 mm [34]) to thick (e.g., 10 mm [26], 20 mm [31]). The influence of the location of the electric potential ground on the electromagnetic force is thus investigated in this study for various workpiece thicknesses. The results are reported for both thin (4 mm) and thick (10 mm) workpieces in Section 5.1. Next, the GMAW conditions of Section 4 are applied. The effect of the assumptions that fundamentally differentiate the three EMF models is examined. Their impact on the current density, magnetic field and resultant electromagnetic force are analysed in Section 5.2. Finally, the effect of these modelling assumptions on the melt pool flow and temperature field (Section 5.3), melt pool geometry (Section 5.4), as well as on the free surface ripples resulting from the impact of the transferred metal drops (Section 5.5), are successively analysed.

5.1. Effect of V-ground location for thin and thick workpiece

The test cases of this section apply to the workpiece alone (no atmosphere and no metal transfer) and the numerical EMF model alone (without thermo-fluid model). The boundary conditions that are not discussed in this section are set as described in Section 4. Figure 5 shows the computed current density vectors, electric potential and electromagnetic force distributions. The plots are presented for two different metal thicknesses: 10 mm in Fig. 5a, b and 4 mm in Fig. 5c–h. Each thickness is combined with two different boundaries for grounding the electric potential: a lateral grounding in Fig. 5a, c, e (left side), and a lower surface grounding in Fig. 5b, d, f (right side). Comparing Fig. 5a and b, it can be seen that for the thick workpiece the ground potential can be at the two studied locations without significantly changing the V-isolines or the $\vec{J}$-distribution in the area where the melt pool is expected to form (i.e., $|x| \leq 5$ mm, $z \leq 3$ mm). On the contrary, Fig. 5c, d show that for the thinner workpiece these two conditions do not give equivalent fields in the region of interest. A comparison between the V-isolines in Fig. 5e (lateral ground) and Fig. 5f (lower surface ground) shows clear differences. Their significant effect on the electromagnetic force can be seen in Fig. 5g and h, plotted along the radial direction x at 2 and 1 mm below the workpiece upper surface (i.e., where liquid alloy could be present). Let us consider for instance the extrema of the electromagnetic field components, which are reached at $x \approx 2$ mm. For the vertical component $(F_{\vec{J}\times\vec{B}})_z$, the absolute value of its extremum at 1 mm (resp. 2 mm) below the surface of the workpiece is about 15% (resp. $\approx$ 70%) larger when setting the electric potential ground at the lateral surface rather than at the lower surface. For the radial component (in these plots $(F_{\vec{J}\times\vec{B}})_x$) the difference is more significant, as the absolute value of its extremum at 1 mm (resp. 2 mm) below the surface is about 30% (resp. $\approx$ 170%) larger when setting the electric potential ground at the lower surface rather than at the lateral surface. These results imply that assumption (ix-(a)) is particularly important to respect when applying the analytical EMF models to thin workpieces, while it could be neglected for thick workpieces when the arc is operated in conduction mode as in this study. Besides, for an electric arc operated in keyhole mode (plasma arc) it is anticipated that this assumption might not be reasonable to circumvent when applying one of the analytical EMF models to a 10 mm thick workpiece, especially when burn-through occurs, since then the region of influence of the EMF force extends deeper into the workpiece.

5.2. Effect of the EMF models on the electromagnetic force

This section focuses on the different EMF models (without thermo-fluid model). The test cases apply to the workpiece alone (no atmosphere and no metal transfer). The computational results presented in the sequel were all obtained for a 10 mm thick workpiece, with the setting of the GMAW test case of Section 4. It was checked in Section 5.1 that the boundary condition $V = 0$ can be set at the lower or at the lateral surface of the 10 mm-thick workpiece without affecting the results, when computing the numerical EMF. It implies that the constraint (ix*) can also be satisfied by the numerical EMF model in the studied test case. Then, the Kou and Sun model differs from the numerical EMF model through (xi) alone, and from the Tsao and Wu model through (ix)/(xii)–(xiii). Figure 6 shows the current density calculated with each of the three EMF models, plotted along the x direction at $y = 0$. In these plots J_x is equivalent to J_r and $x - x_0$ to r. The results are reported at elevations that would be in the melt pool, close to its surface (upper figures at $z = 9.9$ mm) or deeper (lower figures at $z = 8.1$ mm). The plots at the left side show the x-component of the current density while those at the right side show the z-component. It can be seen that the numerical model and the model of Kou and Sun lead to the same results for both J_x and J_z. This is as expected since these two models are based on the same assumptions for determining the electric potential (provided that the boundary conditions are treated consistently). On the other hand, the additional simplifications of the Tsao and Wu model lead everywhere to clear differences in both J_x and J_z. It can be seen that these differences are not systematic. J_x is indeed more than one order of magnitude smaller with the model of Tsao and Wu than with the two other models when $z = 9.9$ mm. On the contrary, it is larger in the vicinity of the arc centre ($x - x_0 = 0$) when $z = 8.1$ mm. The maximum value of J_z is about 30% larger at $z = 9.9$ mm with the model of Tsao and Wu than with the two other models, and it is more than one order of magnitude larger at $z = 8.1$ mm. It implies that the components J_x and J_z do not change with the same proportions when changing from the Tsao and Wu model to any of the two other models. Furthermore, the proportionality factor varies with the position. As a result the simplifications made when predicting J_x and J_z with the model of Tsao and Wu cannot be simply compensated by a constant multiplying factor to recover the more general results of the two other models.

Figure 7 shows the component B_y of the magnetic field along the x direction at $y = 0$ and the elevations $z = 9.9$ mm and $z =$

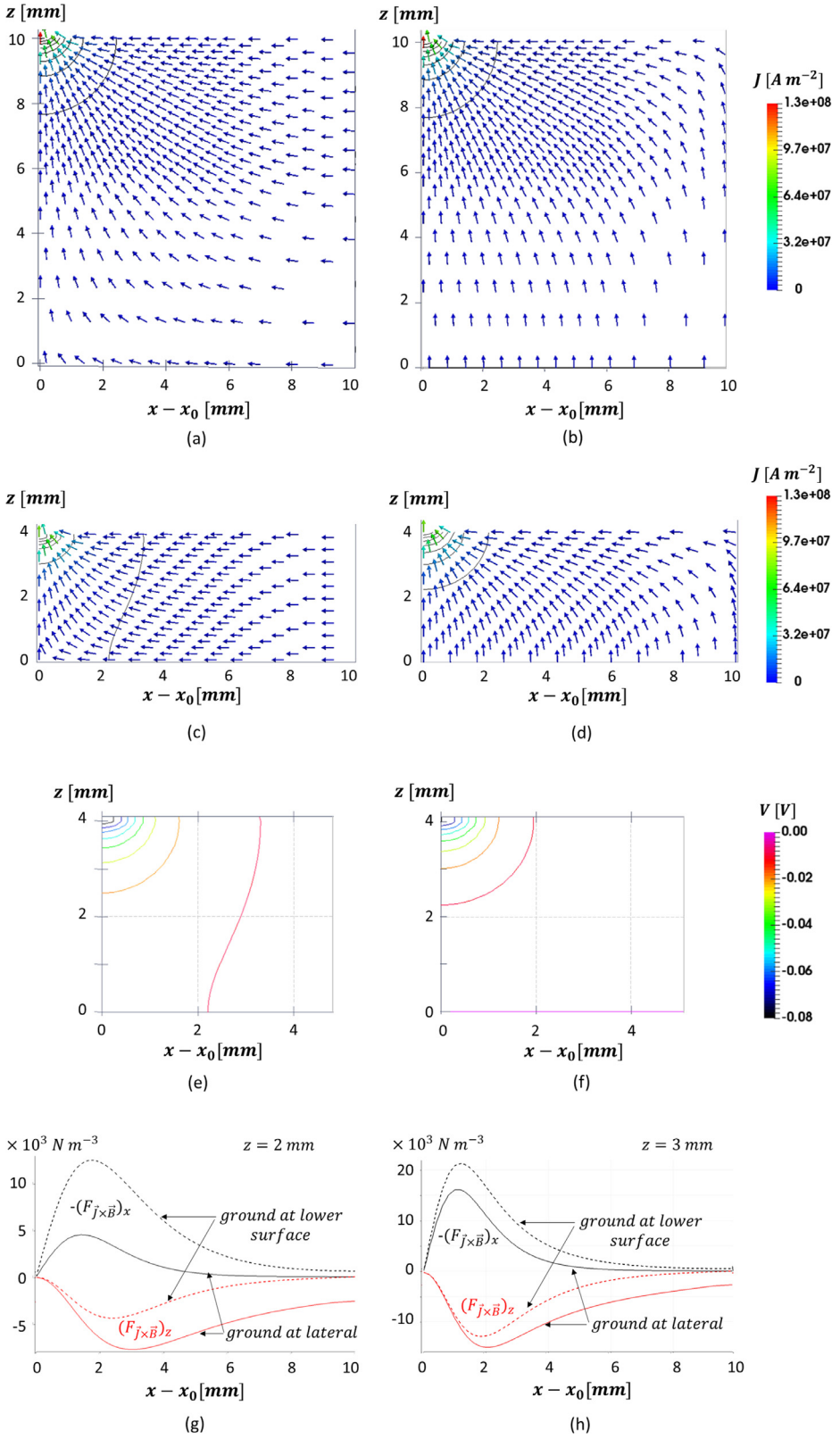

Fig. 5. Solution of the numerical EMF model for (a)-(b): 10 mm and (c)-(h): 4 mm thick workpiece. (a)–(d) : current density vectors; (e)-(f) : electric potential isolines from -0.08 to 0 V with intervals of 0.01 V; with *V* grounded at lateral (left plots) and at the lower surface (right plots). Electromagnetic force along *x* at (g): 2 mm and (h): 1 mm below the upper surface; with solid and dashed lines for ground at lateral and at lower surface, respectively.

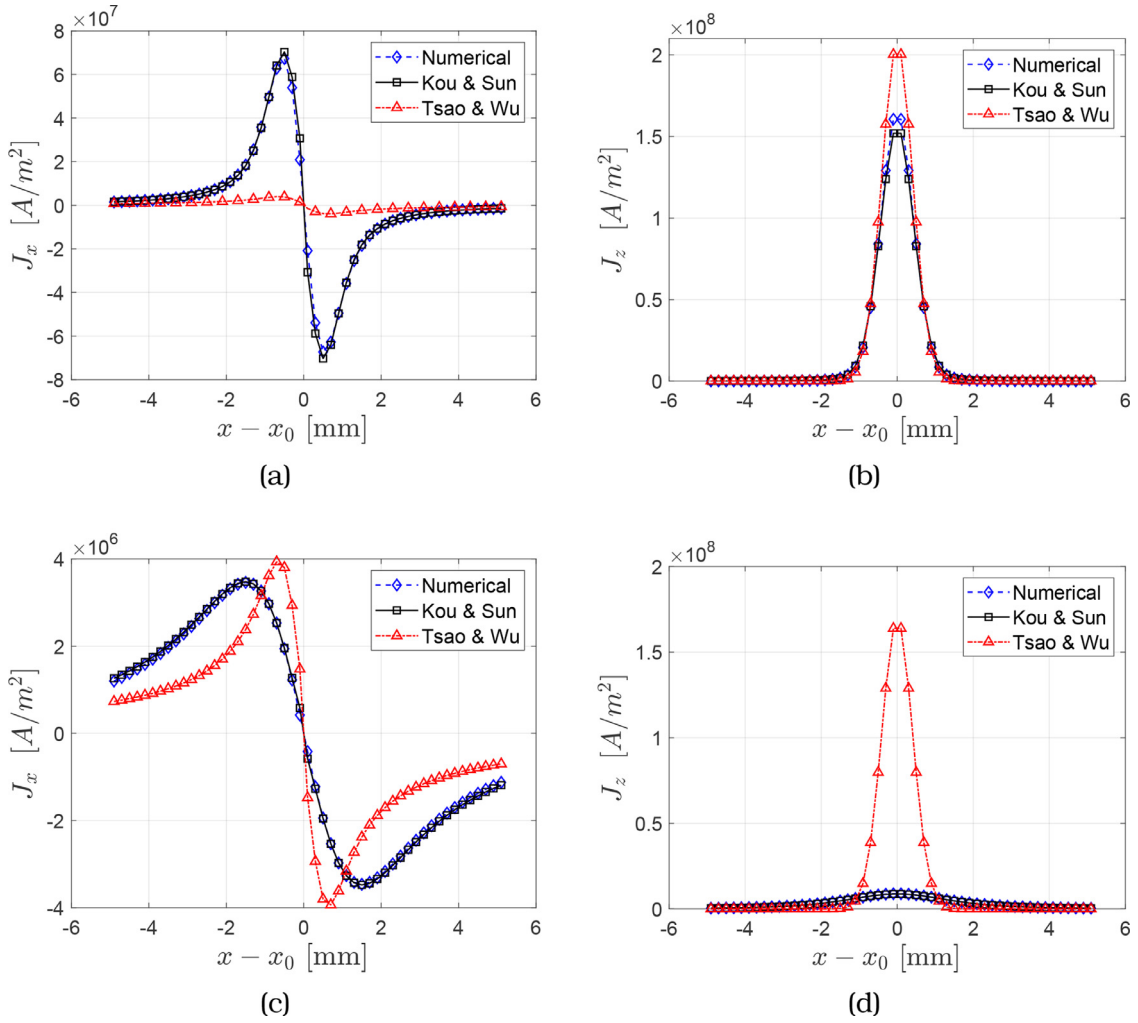

Fig. 6. Current density components at $y = 0$ as functions of the position along x (arc center in $x - x_0 = 0$). Top (a), (b): at $z = 9.9$ mm. Bottom (c), (d): at $z = 8.1$ mm. Left (a), (c): J_x (or here J_r for the analytical EMF models). Right (b), (d): J_z.

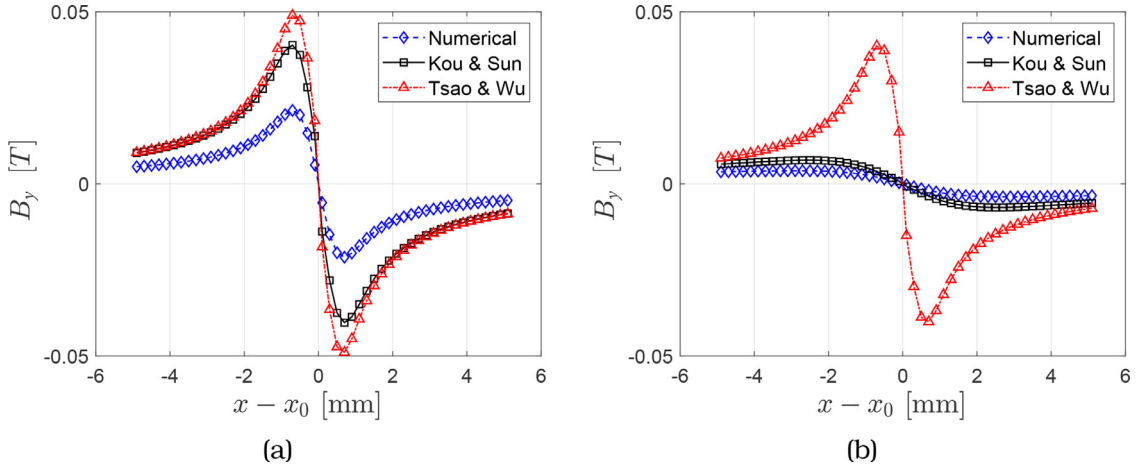

Fig. 7. Magnetic field component B_y as function of the position along x (arc center in $x - x_0 = 0$). (a): at $z = 9.9$ mm. (b): at $z = 8.1$ mm. For the analytical EMF models B_y here corresponds to B_θ.

8.1 mm. In these plots B_y is equivalent to B_θ and $x - x_0$ to r. It can be seen that the model of Tsao and Wu overestimates the magnetic field everywhere compared to the two other models. This overestimation changes amplitude depending on the spatial location. For instance, close to the arc center ($x - x_0 \approx 0$) it is much larger at $z =$ 8.1 mm than at $z = 9.9$ mm. This is a consequence of assumption (xiii) which implies that B decreases linearly with z rather than exponentially. Therefore, here too the simplification made cannot be compensated by a constant multiplying factor to recover the more general results of the two other models. Besides, the mag-

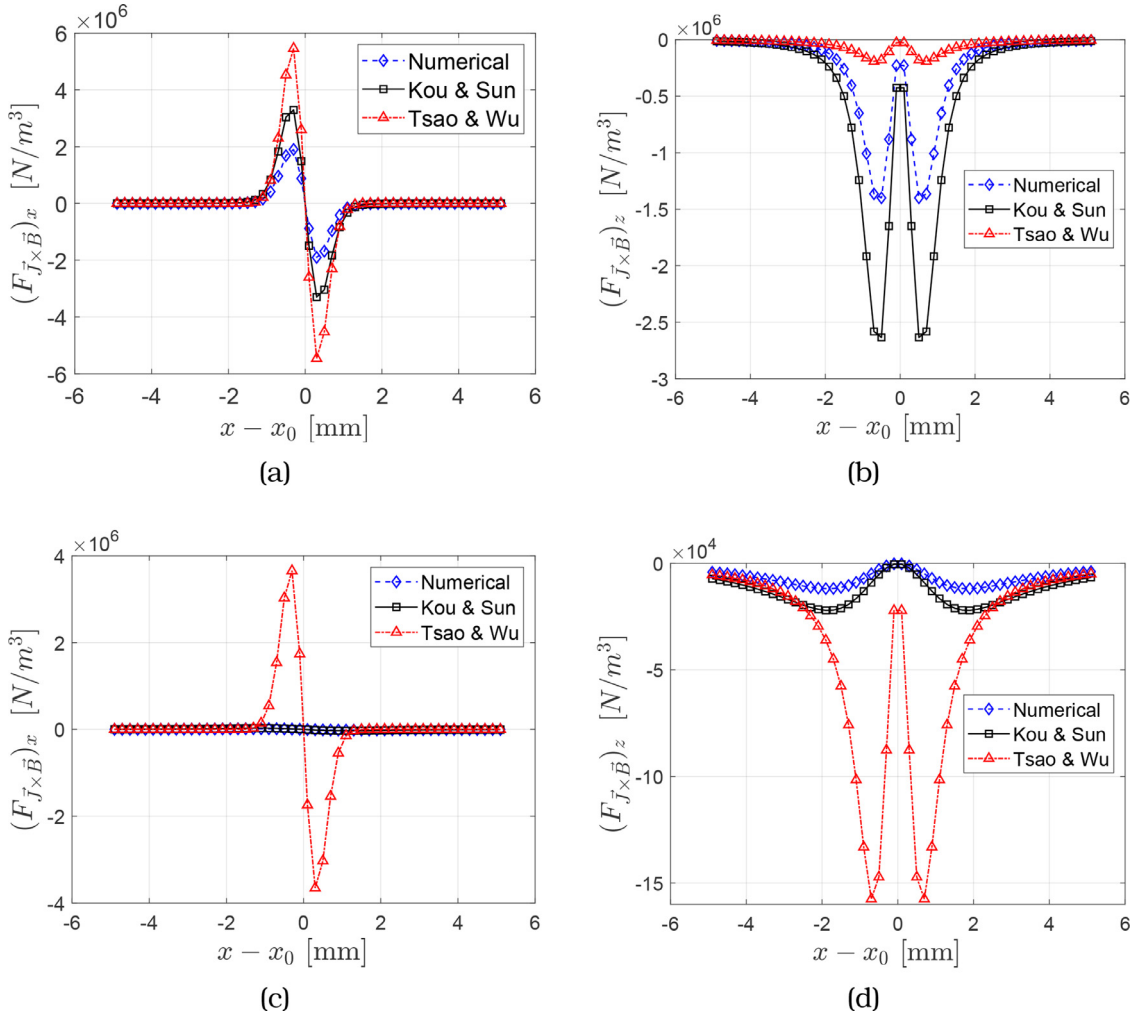

Fig. 8. Electromagnetic force components as functions of the position along x (arc center in $x - x_0 = 0$). Top (a), (b): at $z = 9.9$ mm. Bottom (c), (d): at $z = 8.1$ mm. Left (a), (c): $(F_{\vec{J}\times\vec{B}})_x$ (or here $(F_{\vec{J}\times\vec{B}})_r$ for the analytical EMF models). Right (b), (d): $(F_{\vec{J}\times\vec{B}})_z$ at z.

netic fields computed using the numerical model and the analytical model of Kou and Sun now differ to a significant extent. This is due to the contribution of J_r (J_x in Fig. 6) to B_θ that is ignored in the model of Kou and Sun (see assumption (xi) and the following discussion). The results show that locally this contribution can reach up to 90% of the value of the magnetic field (see Fig. 7(a) at $|x - x_0| \approx 1$ mm). Recall that in this case the model of Kou and Sun is equivalent to the simplified version of the numerical EMF model that computes the magnetic field from the Biot-Savart law. Therefore, the two variants of the numerical EMF model (see Section 1) cannot be considered as equivalent in the context of GMA (nor gas tungsten arc [11]).

Figure 8 shows for each of the three EMF models the x and z components of the electromagnetic force plotted as functions of x relative to the arc centre (in x_0) at $y = 0$ and at the elevations $z = 9.9$ mm and $z = 8.1$ mm. As expected, the results reflect the differences in current density and magnetic field previously observed. It can be seen that the difference in assumptions made in the models of Kou and Sun and Tsao and Wu lead to significant differences for both $(F_{\vec{J}\times\vec{B}})_x$ and $(F_{\vec{J}\times\vec{B}})_z$. While in the studied example the model of Kou and Sun overestimates the components of the electromagnetic force by a factor of about two compared to the numerical model, no clear proportionality is seen between the model of Tsao and Wu and the two others. For instance, let us compare the absolute extrema reached with the model of Tsao and Wu compared to the numerical model. For the component $(F_{\vec{J}\times\vec{B}})_x$ the extrema are almost three times larger at $z = 9.9$ mm, and more than two orders of magnitude larger at $z = 8.1$ mm. While for the component $(F_{\vec{J}\times\vec{B}})_z$ they are about five times smaller at $z = 9.9$ mm, and one order of magnitude larger at $z = 8.1$ mm. In other words, the modelling assumptions (xii)-(xiii) (Section 2.2) change not only the amplitude of the electromagnetic force but also the proportion of its components, furthermore in a space-dependent way.

5.3. Effect of the EMF models on the melt pool flow and temperature field

The calculation results presented in the following were computed for the complete GMAW test case with workpiece, atmosphere and transferred metal drops. They were obtained combining the thermo-fluid model with each of the EMF models. The EMF model is the only element varied in the next comparisons. The simulation results are from now time-dependent. Time $t = 0$ s is the time when the arc heat source is switched on. The metal transfer starts at $t = 0.03$ s and continues with the drop frequency $f_{drop} = 156$ Hz. It was checked that at time $t = 8$ s the melt pool was already fully developed with each of the models (see Section 5.4). The computations were conducted up to the time $t = 12$ s. Look-

ing at the simulation results over several cycles of metal transfer while the melt pool is fully developed, it can be observed that in a large part of the liquid alloy the computed fields present almost no variation with time (see supplementary material, movies S2-S5c). However, this observation does not apply to the drop impact area or to the free surface area due to the propagation of ripples issuing from drop impact. In these two last areas the flow, in particular its velocity, shows some periodicity related to the metal transfer periodicity (see also Sections 5.3, 5.5). However, possible random fluctuation of the mean flow is not investigated in the scope of this study.

Figure 9 presents, at time $t = 12$ s, velocity vectors computed in the liquid alloy with each of the three EMF models. Figure 9a shows top-view images with the melt pool free surface in grey color, and Fig. 9b presents side view images in a longitudinal section at $y = 0$ (symmetry plane). The arc axis is aligned with the z-axis and passes through $x_0 = 50$ mm, and $y_0 = 0$ mm. At this location it can be seen in both Fig. 9a and b that the velocity vectors have different orientations with the different EMF models. This is related to the dynamics of the flow during the drop impact cycle, which is discussed in Section 5.5. Figure 9a shows that at the free surface, in a radius of approximately 3 mm about the arc axis, the velocity vectors are oriented radially outward due to the combined effect of the thermocapillary force (outward), the x, y-components of the electromagnetic force (inward radial contribution), and the dynamics of the flow related to the ripples caused by the drops (outward). The black line plotted at the melt pool surface in Fig. 9a represents the temperature isoline $T = 1850$ K, across which the thermocapillary force of an iron alloy containing 40 ppm sulfur changes sign. It can be seen that at the free surface the flow changes direction across that line, and that recirculation vortices form at the rear part of the melt pool. When observed over a time period while the melt pool is fully developed, this isoline is quasi-steady with negligible oscillation (see supplementary material S2). It is also observed in Fig. 9a that the shape of this isoline is different with the different EMF models, in particular the transition shoulder in the vicinity of $x = 40$ mm. Its shape is smoother with the Kou and Sun model than with the numerical EMF model, while is it more abrupt with the Tsao and Wu model. It implies that the EMF models have also different effects on the thermocapillary flow.

Figure 9b shows that under the free surface the melt pool flow is very different depending on the EMF model, as highlighted by the white arrows indicating recirculation regions. Examining the fully developed melt pool as time evolves, it can be observed (see supplementary movies S3) that the recirculation regions remain the same for the most part, except near the arc center ($x = 50$ mm) where the flow pattern shows dynamic evolution related to the periodic drop impact. Behind the arc axis ($x \lesssim 50$ mm) a very large recirculation is observed with the Kou and Sun model. It is associated with a downward melt pool flow at the arc center that is characteristic of a leading order electromagnetic force. With the numerical EMF model this recirculation region is smaller, while with the Tsao and Wu model it is not observed. On the contrary, a recirculation rotating in the other direction (seen counterclockwise in Fig. 9b), which is characteristic of a leading order thermocapillary force, is observed with the model of Tsao and Wu, as well as with the two other models but then further behind the arc. It is largest with the Tsao and Wu model, and extends from the arc region to far downstream up to about $x = 40$ mm (or P3), where the thermocapillary force changes direction. It has a smaller size with the numerical EMF model as it faces the first recirculation in the vicinity of $x = 45$ mm (or P1). The smallest size is given by the Kou and Sun model. In that case the reverse direction swirls confront at $x \approx 47.5$ mm (or P2). The assumptions (xi) and (ix)/(xii)–(xiii) that differentiate the three EMF models thus introduce simplifications with significant consequences on the melt pool flow. It was seen in Fig. 8a that the electromagnetic force components have an amplitude that depends on the EMF model close to the arc axis ($|x - x_0| \lesssim 4$ mm). The electromagnetic force component $(F_{\vec{J}\times\vec{B}})_z$, which is oriented downward, has the largest amplitude with the Kou and Sun model and the smallest amplitude with the Tsao and Wu model (Fig. 8b). These differences are consistent with the differences in recirculation flow observed under the free surface in Fig. 9b in the arc axis area ($|x - x_0| \lesssim 4$ mm). In that same region the amplitude of the radial component (oriented inward) of the electromagnetic force about the arc axis is smallest with the numerical EMF model (resp. largest with the Tsao and Wu model; see Fig. 8a). Thus, it decelerates the less (resp. the most) the thermocapillary flow. However, this seems to be in contradiction with the radial extent of the melt pool that is wider with the Tsao and Wu model than with the numerical EMF model (Fig. 9a, and 14 d). Moreover, Fig. 8 shows that for each of the EMF models the electromagnetic force is negligible at more than 5 mm from the arc centre. Thus the differences in flow pattern in the region of P1 and P2 are not simply direct effects of the electromagnetic force. The problem becomes more complex by the presence of both solid/liquid and liquid/gas interfaces that interact with the thermal convection. Free-surface oscillations are also known to influence the thermocapillary flow [63]. The indirect effect of the electromagnetic force on the flow dynamic due to differences in melt pool morphology (Section 5.4) and on free surface oscillation during drop impact and coalescence (Section 5.5) need also to be considered.

Figure 10 shows the evolution over time of the maximum fluid velocity, $u_{\max}$, computed at the melt pool free surface (isosurface $\alpha f_l = 0.5$) for the different EMF models. The time interval reported, $11.95 \leq t \leq 12$ s, includes 8 cycles of metal transfer. It can be seen that that $u_{\max}$ follows a periodic pattern with a frequency corresponding to the metal transfer frequency. The extrema reached by $u_{\max}$ are almost the same for the different EMF models. During each cycle of metal transfer, $u_{\max}$ varies between about 1.6 to 0.4 m s^{-1}. Figure 10 shows that the time $t = 12$ s corresponds to the end of a cycle, thus the maximum velocity of about 0.4 m s^{-1} in Fig. 9. The minimum value of $u_{\max}$ is thus 50 times larger than the welding travel speed ($U_{tr} = 0.008$ m s^{-1}), and the maximum value is about 20% above the initial drop velocity ($|u_{drop}| = 1.3$ m s^{-1}). The root mean square of $u_{\max}$ was calculated over the reported time interval, leading to the values indicated in Fig. 10 for each EMF model. The RMS value obtained with the numerical and the Kou and Sun models are very similar, while with the Tsao and Wu model it is about 20% lower. A possible reason for this difference is proposed below examining the temperature field. Besides, the evolution of $u_{\max}$ over a metal transfer cycle follows different patterns depending on the EMF model, as can be observed in Fig. 10. With the numerical and Kou and Sun models it goes up and down two times, while with the model of Tsao and Wu there is only one peak per cycle. This might be related to the primary and secondary ripples discussed in Section 5.5.

Figure 11 visualizes the computed temperature distribution at the symmetry plane $y = 0$ and at time $t = 12$ s. It can be seen that the three EMF models result in different convection of the heat transferred to the workpiece by the arc and the metal drops. The heat is convected deeper into the material and over a wider extend with the Kou and Sun model compared to the numerical EMF model. It shows that the overestimation of the amplitude of $(F_{\vec{J}\times\vec{B}})_z$ made by the Kou and Sun model due to assumption (xi) through neglecting the contribution of J_r to B_θ enhances the thermal convection towards the melt pool depth. With the model of Tsao and Wu the heat transferred to the material is instead confined to the close vicinity of the free surface. It shows that for this EMF model the underestimation of $(F_{\vec{J}\times\vec{B}})_z$ in the upper part of the melt pool

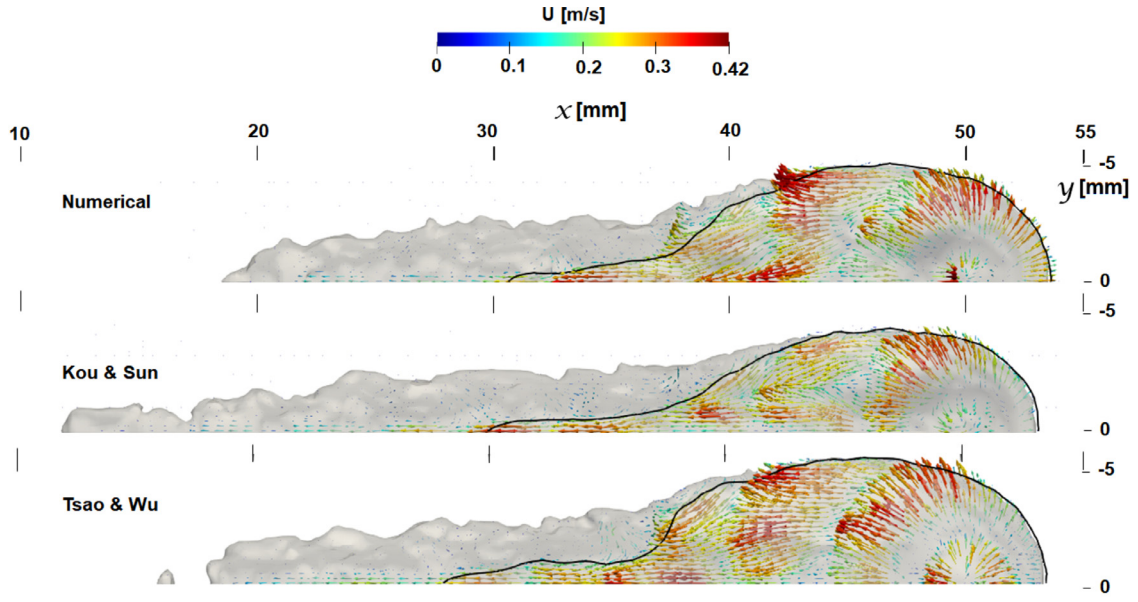

(a) Top view

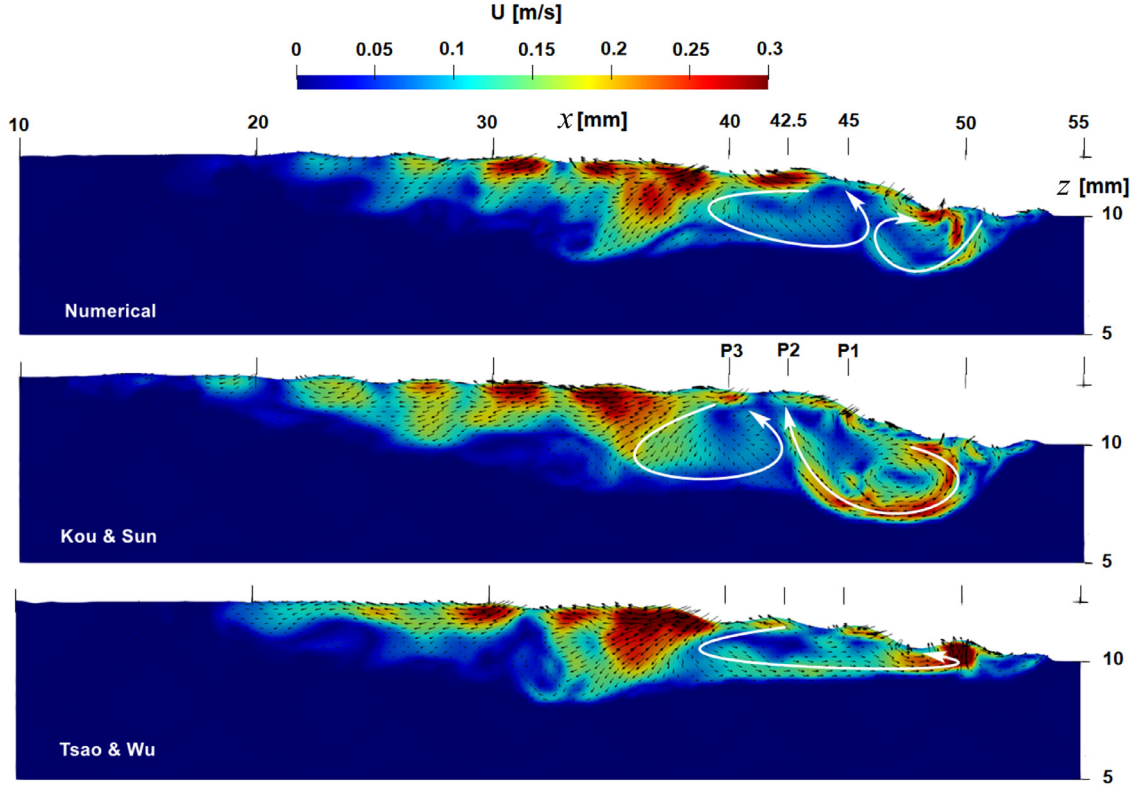

(b) Side view.

Fig. 9. Velocity fields computed in the melt pool at $t = 12$ s with the different EMF models. In (a) the free surface isosurface is in grey. The black line represents the isotherm $T = 1850$ K.

(by a factor 5 in $z = 9.9$ mm, see Fig. 8b) has a larger effect than its overestimation in the lower part (by a factor 10 in $z = 8.1$ mm, Fig. 8d).

The maximum temperature of the metal is also affected by the EMF model used. Its value is about 2800 K with the numerical EMF model and the Kou and Sun model, and about 2500 K with the Tsao and Wu model. These values, that are at the free surface, are at least 300 K lower than the vaporization temperature of the main constituents of the studied alloy. The computed effect of vaporization is insignificant for the melt pool in terms of both energy and mass loss. It confirms that material loss can be neglected, as done in the model (Section 3.1). Besides, a higher maximum temperature is known to strengthen the thermocapillary force, and is expected to result in a larger fluid velocity. Thus, it could explain

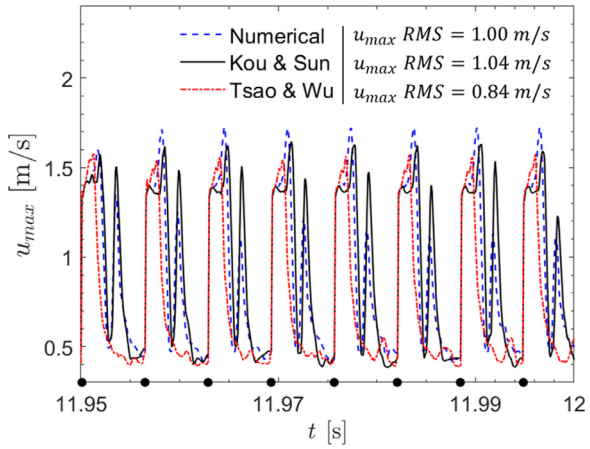

Fig. 10. Evolution over time of the maximum fluid velocity computed at the melt pool free surface with the different EMF models. • : instant of metal drop injection in the computational domain. RMS: Root Mean Square.

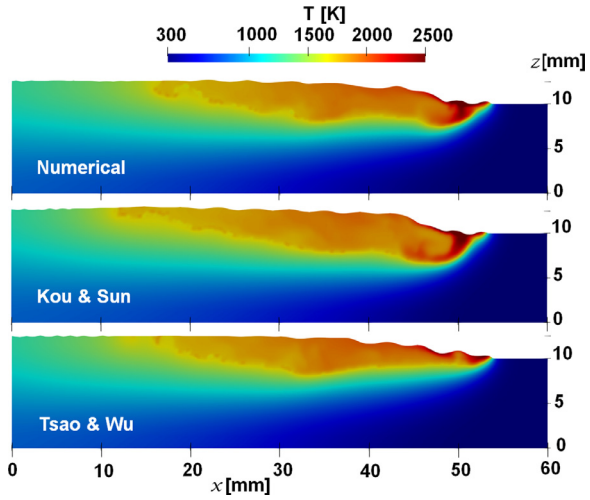

Fig. 11. Temperature distribution at the symmetry plane ($y = 0$) at $t = 12$ s with the different EMF models.

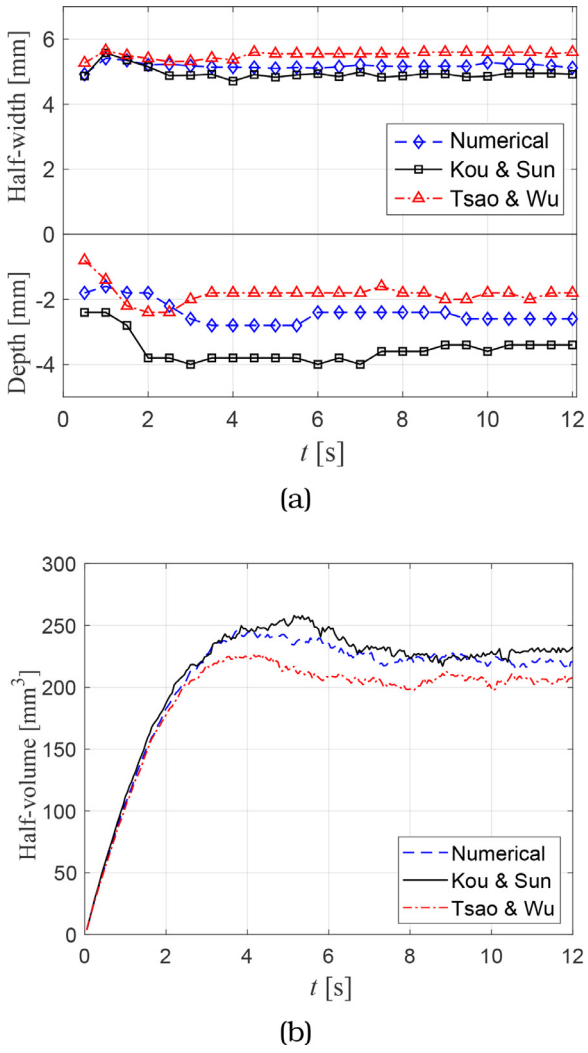

Fig. 12. Evolution over time of the predicted melt pool (a) half-width, depth and (b) half-volume.

why the RMS value of $u_{\max}$ obtained with the Tsao and Wu model is lower than with the two other models.

5.4. Effect of the EMF models on the melt pool geometry

Figure 12 presents the time evolution of the melt pool half-width, penetration depth and half-volume computed with the three EMF models. The results from the different models share in common that at the start of the process the melt pool width and volume increase almost linearly for about 1 s until the trailing edge of the initially circular melt pool begins to develop. The melt pool half-width and penetration depth reach a stable condition after approximately 4 s. However, the melt pool length and volume require longer time to stabilize. The increase in melt pool volume is followed by a decrease at $t \approx 6$ s due to the rapid cooling when the re-solidification of the trailing edge starts. The length and volume expand over a longer time before reaching a quasi-steady condition at $t \approx 8$ s. The results reached at fully-developed melt pool show that the three EMF models lead to different melt pool dimensions. The model of Tsao and Wu leads to a wider and shallower melt pool with smaller volume than the two other EMF models. The model of Kou and Sun instead produces a narrower and deeper melt pool with a volume slightly larger than the numerical EMF model. These geometrical differences result from the distinct effect on the thermal flow of the different simplifying assumptions underlying the EMF models studied. For instance, the most shallow melt pool observed with the model of Tsao and Wu is a consequence of the quasi-absence of convective recirculation of alloy under the arc as a result of the underestimation of $(F_{\vec{J}\times\vec{B}})_z$ in the upper part of the melt pool. It can also be seen that with the model of Tsao and Wu (resp. Kou and Sun) the reduced (resp. increased) melt pool depth is not balanced by the increased (resp. reduced) width since the melt pool volume is smaller (resp. larger) than with the numerical EMF model while the total amount of heat input and its space-distribution (Eq. (32)) is the same for all the cases. The change in force balance due to the simplifying assumptions (xi) and (ix)/(xii)-(xiii) therefore changes also the fraction of heat transferred to the workpiece that is used to melt the alloy.

Figure 13 compares the melt pool geometry computed with each of the three electromagnetic models, at time $t = 12$ s. The top-view images of Fig. 13a show that the largest melt pool width (at section AA') is reached downstream the arc center (located at $x = 50$ mm) at rather similar locations with the numerical EMF model and with the Kou and Sun model, while it is further away with the model of Tsao and Wu. The transition to the tail region is closer to section AA' with the Kou and Sun model than with the two other ones as the front area is then not only narrower

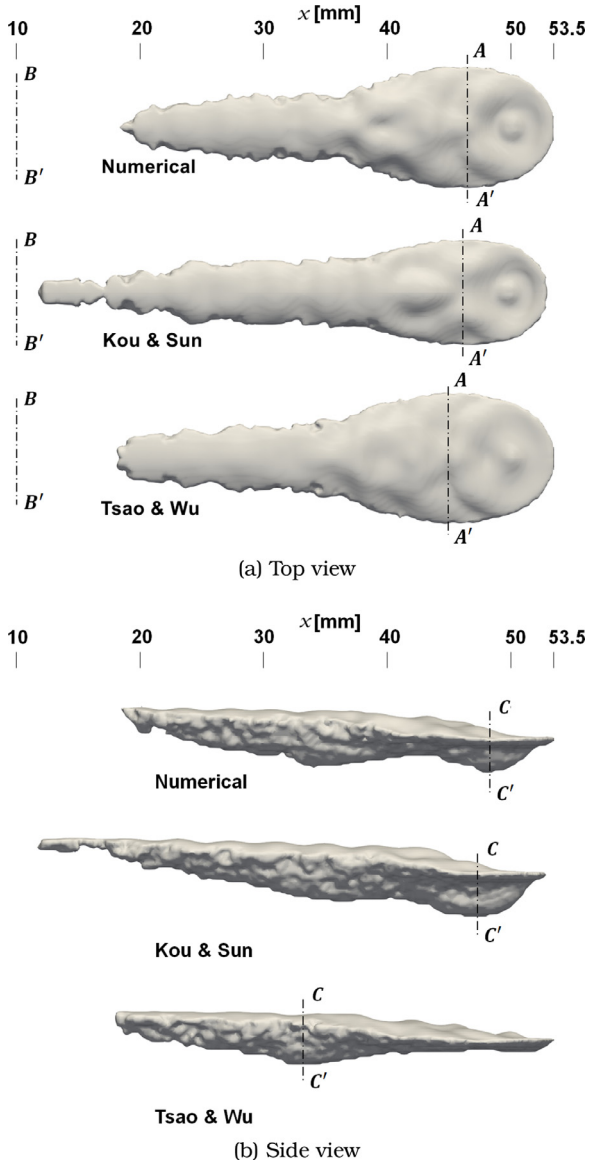

Fig. 13. Melt pool geometry computed with each EMF model; $t = 12$ s.

but also shorter. The side view images in Fig. 13b show that the model of Tsao and Wu leads to a very different melt pool shape, compared to that of the other models. The largest melt pool depth (at section CC') is indeed reached much further downstream the arc center with this model than with the other ones. As noticed in Section 5.3, with this model the largest penetration depth is not governed by the same effects as for the other models. For the two other EMF models the deepest melt pool depth is reached under the arc at $x_0 = 50$ mm. According to the recirculation pattern it is believed to be mainly governed by the electromagnetic force (combined with the metal transfer). With the Tsao and Wu model the largest depth is reached at $x \approx 35$ mm. There, the electromagnetic force is known to be negligible. Thus, these results show that the change in proportion of the force components $(F_{\int \vec{\jmath} \times \vec{B}})_x$ and $(F_{\int \vec{\jmath} \times \vec{B}})_z$ observed in Fig. 8 when changing from e.g., the numerical EMF model to the Tsao and Wu model turn out to be large enough to induce drastic changes in the predicted melt pool morphology.

Figure 14 (a)-(b) present macrograph images of the bead along the longitudinal and transverse directions. Figure 14a shows the uniformity of the penetration depth and the reinforced bead height. Figure 14b visualizes the fusion boundary used for comparison with the computational results obtained at time $t = 12$ s with the different EMF models. Experimental measurements are also reported in Table 6 for three different samples. The accuracy of the measurements was evaluated to be ±0.1 mm due to the uncertainty in positioning the fusion boundary. The values computed with the different EMF models are also reported in this table. Their uncertainty is evaluated based on the mesh cell-size to be equal to ±0.1 mm. The computed boundaries of the reinforced bead plotted in Fig. 14c were extracted from the re-solidified surface (defined by the isosurface $\alpha = 0.5$) at the section BB' (shown in Fig. 13a). The numerical EMF model and the Tsao and Wu model are in good agreement with the experimental data, the relative error being less than 4% compared to the average experimental value. With the Kou and Sun model the relative error is larger, reaching approximately 16%. Since the added mass (and thus volume) from the wire feed is the same for all the simulated cases, the increased reinforced height with the Kou and Sun model is correlated to the reduced melt pool width. The melt pool depth and width reach their maximum values at different distances from the arc center. The computed edge of the fusion zone is defined by the solidus isotherm. The melt pool width compared to the experimental data in Fig. 14d is plotted in section AA, and the penetration depth compared in Fig. 14e is plotted in section CC (see Fig. 13). It can be seen that the (maximum) width predicted with the numerical EMF model is in good agreement with the experimental results. With the Tsao and Wu model it is overestimated whereas with the Kou and Sun model it is underestimated. The maximum relative error between the numerical simulations and the experimental results is about 15%. Figure 14e shows that the maximum penetration depth obtained with the numerical EMF model is in very good agreement with the experimental results, with a difference of less than 3%. This is simply a direct consequence of the adjustment of the closure parameter $\sigma_{arc,\vec{\jmath}}$, as explained in Section 3.2. Nevertheless, the morphology of the fusion zone simulated using the numerical EMF model slightly differs from the experimental data. Besides, it can be seen that the penetration depth is overestimated by approximately 30% with the Kou and Sun model and underestimated by approximately 30% with the Tsao and Wu model. These differences are significant. Furthermore, while the depth to width ratio is correctly reproduced by the numerical EMF model, it is not by the two other models. The GMAW example of this study therefore shows that assumptions (ix)/(xii)-(xiii) as well as (xi) alter the leading order physics predicted in the melt pool.

Table 6
Bead dimensions measured experimentally, and computed with each EMF model.

		Height [mm]	Width [mm]	Depth [mm]
Experimental	Sample 1	2.5±0.1	10.2±0.1	2.6±0.1
	Sample 2	2.45±0.1	10.3±0.1	2.7±0.1
	Sample 3	2.6±0.1	10.4±0.1	2.5±0.1
Average exp. value:		2.5±0.1	10.3±0.1	2.6±0.1
Computed	Numerical	2.6±0.1	10.1±0.1	2.6±0.1
	Kou & Sun	2.9±0.1	8.8±0.1	3.4±0.1
	Tsao & Wu	2.5±0.1	10.8±0.1	1.9±0.1

5.5. Effects of the EMF models on the ripples from drop impact

The general dynamics of the surface is first discussed before going into detailed comparisons with the three EMF models. Figure 15 presents symmetry plane views of the melt pool computed with the numerical EMF model. The plots show the drop impact area at different instances in time chosen to highlight particular features within a period of metal transfer when the melt pool is fully developed. When a metal drop is transferred (see A) and enters the melt pool (B) a depression forms (C) until reaching

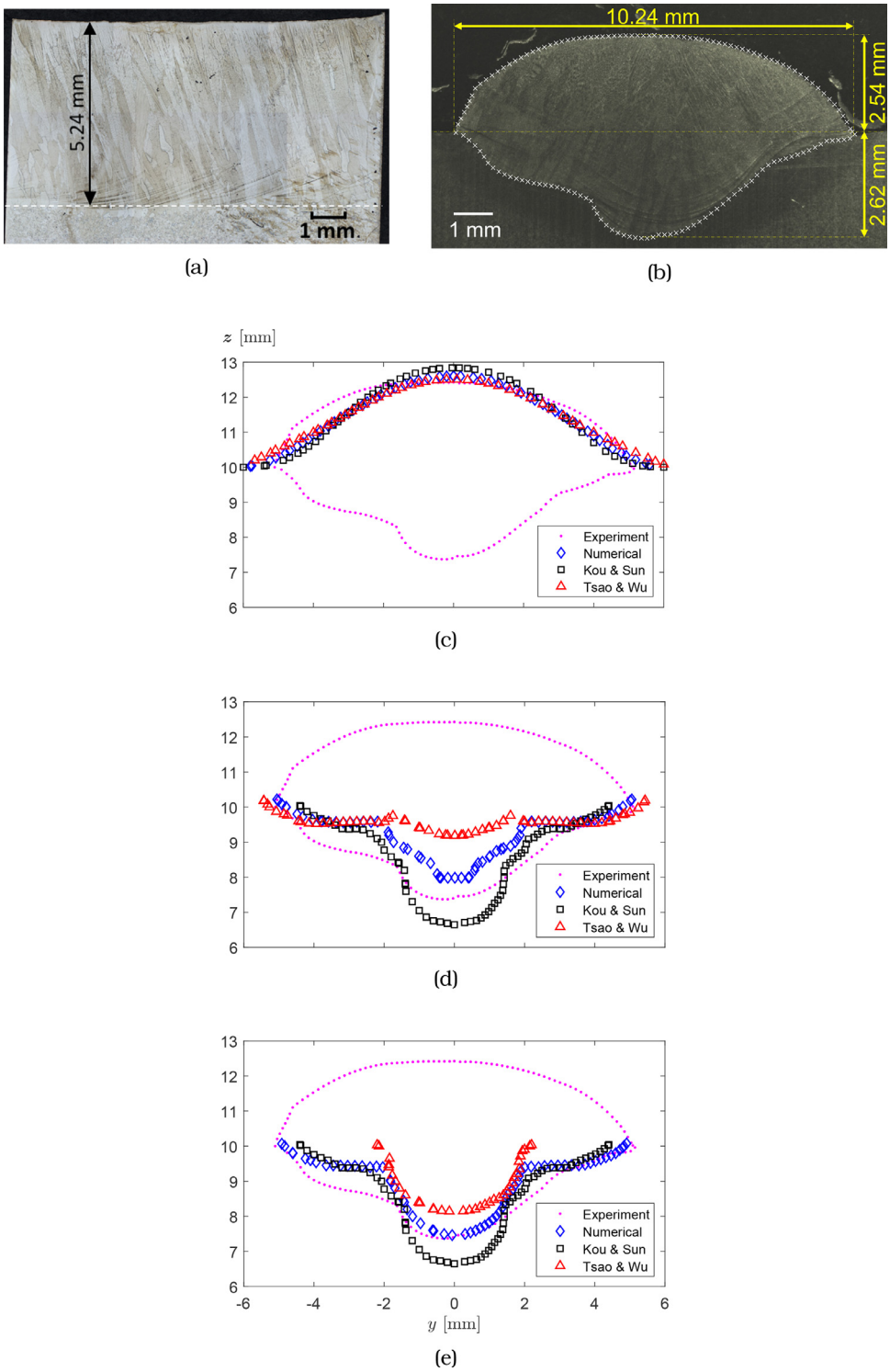

Fig. 14. Metallographic image showing the solidified fusion zone and reinforced bead in a section (a) longitudinal and (b) transverse. Comparison between the experimental bead contour extracted from (b) and the fusion zone contour computed with the three different EMF models showing the (c) bead reinforced height in section *BB'*, (d) width in section *AA'*, and (e) penetration depth in section *CC'*.

the maximum depression (D). The metal pushed away causes the formation of a primary ripple that moves away from the point of drop impact as time evolves (see supplementary movie S4). Next, the free surface starts restoring (E) with a central jet formation (F) resulting in a secondary ripple (G) that is still partially present when the next drop is transferred (H).

Figure 16 compares the evolution over time of the liquid alloy top-most surface, which includes both the free surface and the drop. It is computed with the different EMF models and is reported at the arc centre. This location coincides with the location of the drop impact. The figure shows two cycles of metal transfer taking place when the melt pool is fully developed. The plots start when

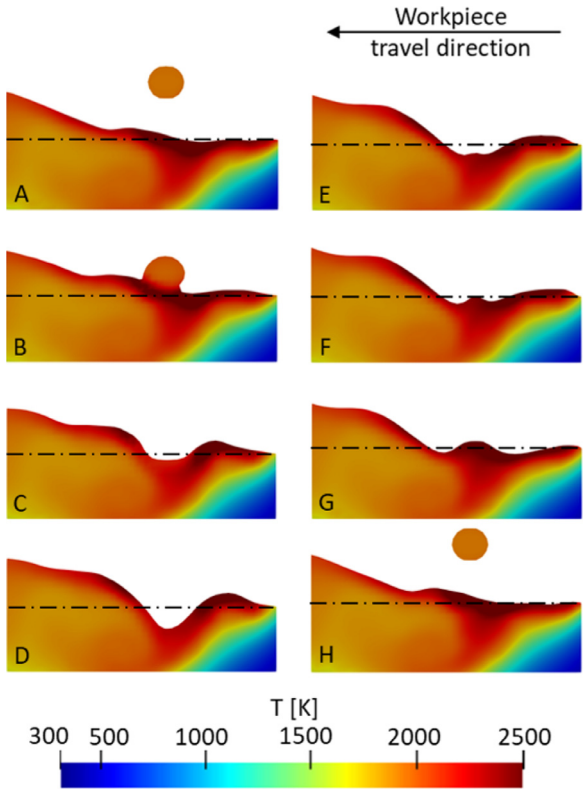

Fig. 15. Melt pool free surface deformation computed with the numerical EMF model and plotted at various instances in time within a metal transfer period. The dashed-dotted line indicates the original elevation of the workpiece upper surface (at $z = 10$ mm). The blue/brick color corresponds to a temperature range below/above the melting temperature (1712.5 K). (For interpretation of the references to colour in this figure legend, the reader is referred to the web version of this article.)

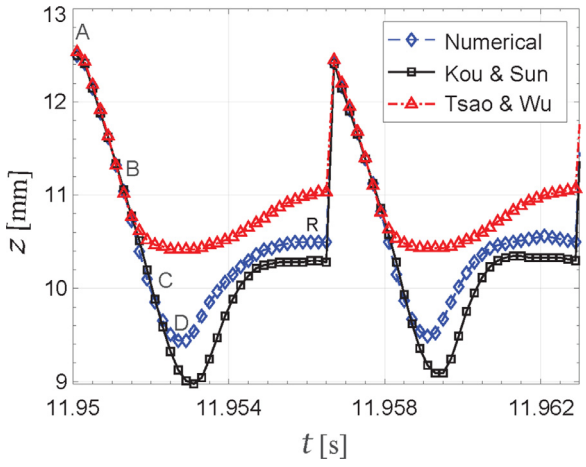

Fig. 16. Evolution over time of the free surface elevation at the arc centre, computed during two cycles of metal transfer with each of the three EMF models. The original elevation of the workpiece upper surface is in $z = 10$ mm. (For interpretation of the references to colour in this figure legend, the reader is referred to the web version of this article.)

the drop is injected into the computational domain (in A, as in Fig. 15). A sudden increase in top-most surface elevation can be seen when a new drop is inserted since at this instant the height reported in Fig. 16 includes the diameter of the drop (1.2 mm) and the space between the drop and the free surface. In B the drop has partially entered the free surface (similar to B in Fig. 15), and in C it is totally immersed and has initiated a depression at the melt pool free surface. Figure 16 shows that the depression (in D, as in Fig. 15) is the deepest with the Kou and Sun model, with a free surface lowering reaching about 1.3 mm, whereas the Tsao and Wu model leads to the shallowest lowering of only 0.5 mm. Compared to the numerical EMF model the restored height (in R) is 0.5 mm higher with the Tsao and Wu model, while it is 0.2 mm lower with the Kou and Sun model. Furthermore, the time needed to reach the deepest depression after the drop impact is the longest with the Kou and Sun model, while it is almost the same with the two other models. On the contrary, the time needed to restore the elevation as prior to impact (e.g., from D to R) is the shortest with the Kou and Sun model while it is the longest with the Tsao and Wu model. These variations are caused by the force balance at the free surface and the thickness of liquid alloy under the impact point, which are different for each of the three EMF models (see previous sections). The effect on the amplitudes and propagation of the ripples is now examined as they move away from the point of drop impact.

Table 7
Velocity along the x-direction of the crest of the ripples moving towards the rear part of the melt pool, for each EMF model.

	Crest x-velocity [mm s^{-1}]					
	Set $\mathcal{A}$			Set $\mathcal{B}$		
Model	mean	max.	min.	mean	max.	min.
Numerical	856.6	909.1	769.2	918.4	11250.0	714.3
Kou & Sun	836.7	1000.0	555.5	1058.5	1428.6	714.3
Tsao & Wu	761.2	909.1	666.6	–	–	–

The primary ripple that moves towards the front side of the melt pool is reflected as it reaches the liquid/solid transition region (see S4). Along this back and forth travel, the amplitude of the ripple progressively attenuates. Towards the rear side of the melt pool, the propagation is more complex. It is now examined in more details. In the computations with the numerical and the Kou and Sun EMF models, primary and secondary ripples are observed to travel away from the point of drop impact (see S5a-b). With the model of Tsao and Wu, no secondary ripple is seen to travel away (S5c). The speed of the crests of the ripples computed with each of the models was evaluated along the travel direction, after the arc centre, from the time $t = 11.95$ s to $t = 12$ s. This time interval includes 8 cycles of metal transfer. The evaluation was made by sampling the times of passage of the crests, first at $x = 46$ mm and next at $x = 45$ mm. For the cases with secondary ripples, as the primary and the secondary ripples alternate, the crests successively detected were alternately distributed in a set $\mathcal{A}$ and a set $\mathcal{B}$. However, as it was difficult to determine whether the ripples passing at $x = 46$ mm were primary or secondary, the correspondence between set ($\mathcal{A}$ or $\mathcal{B}$) and ripple type (primary or secondary) could not be established. Nevertheless, the minimum, maximum and mean crest velocities were calculated for each set over the time interval above mentioned. The results are reported in Table 7. It can be seen that in all the cases the ripples move much faster than the welding travel speed, $U_{\mathrm{tr}} = 8$ mm s^{-1}. They also show that the primary ripples predicted by the model of Tsao and Wu are on average slightly slower (about 10%) than the slowest set ($\mathcal{A}$) of ripples predicted by the two other models. Finally, it can be seen that when both primary and secondary ripples are present, they have different average velocities. It implies that a $\mathcal{B}$-ripple might catch up with the $\mathcal{A}$-ripple ahead of it.

Figure 17 presents the free surface elevation computed with the different EMF models and plotted at three locations along the travel direction over a period of 0.05 s. These locations are positioned at increasing distances after the arc center, as shown in Fig. 17a: 5 mm (point P1), 7.5 mm (P2) and 10 mm (P3). It can

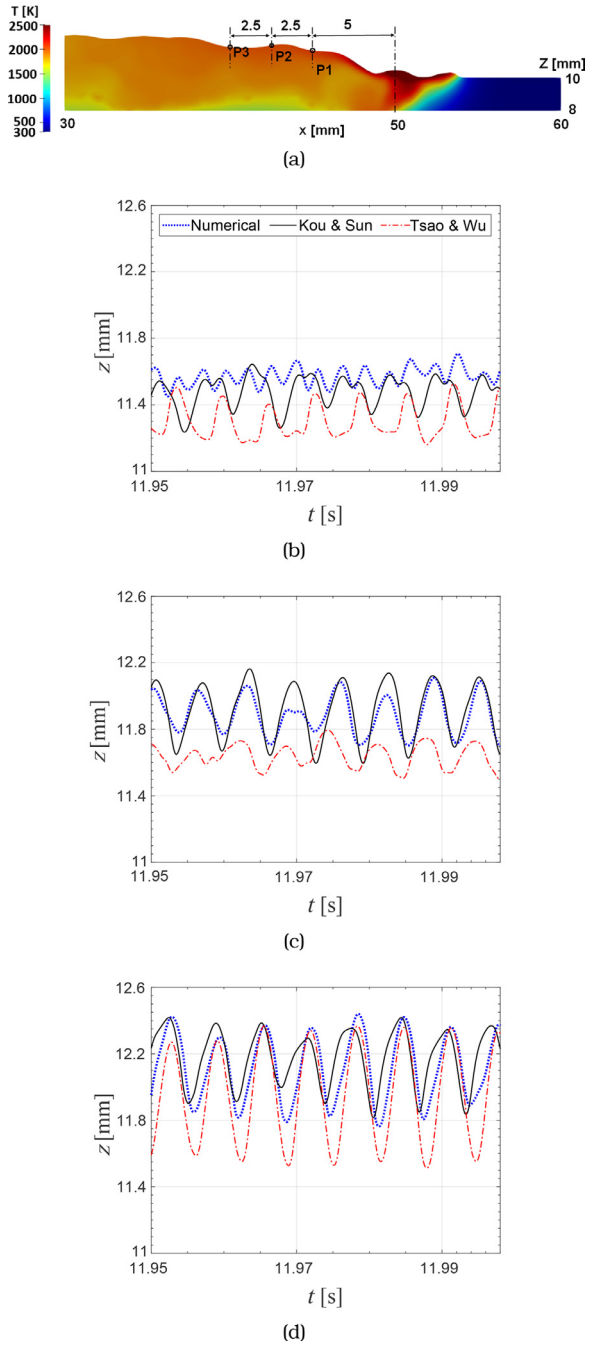

Fig. 17. Surface oscillation at the melt pool free surface (observed in the reference frame of the heat source). (a) Location of the monitoring points P1, P2 and P3. Free surface elevation z at (b) P1, (c) P2, and (d) P3.

be seen in Fig. 17b that with the Tsao and Wu model a ripple passes in P1 at the frequency of 156 Hz (i.e., the drop transfer frequency). When using the numerical EMF model and the Kou and Sun model the number of ripples passing P1 at that frequency is doubled. Two ripples can clearly be distinguished with the numerical EMF model while partial overlap is observed with the Kou and Sun model. These differences are related to the location of drop impact on the secondary ripple (see S5a-c). It occurs on the crest of the secondary ripple with the model of Tsao and Wu (therefore the primary and secondary ripples are merged). With the two other models, the drop falls over a longer distance before reaching the free surface whose elevation is then lower just prior to impact (see Fig. 17). This delay permits the secondary ripple to travel, so that the drop impact takes place at some distance after the passage of the secondary crest. In the computations with the Kou and Sun model the delay is even larger than with the numerical EMF model. The delayed impact generates a surface elevation with two crests that move away from the point of impact. These two crests are more or less differentiated depending on the delay and on the point of observation (as they travel at different speeds). Figure 17c shows that when reaching further away to point P2, the primary and secondary ripples are merged for these two last models. The remaining differences are a small phase shift and the slightly larger crest elevation with the Kou and Sun model compared to the numerical one. The amplitude of the ripples predicted by the Tsao and Wu model is still clearly the smallest at P2 while it becomes the largest at P3. Ripples could be expected to lower their amplitude along their travel away from the arc center due to energy dissipation. But this is not the case here. With the numerical EMF model the ripple amplitude increases between P1 and P2, and further between P2 and P3. With the Kou and Sun model no noticeable change in ripple amplitude is seen between P2 and P3. Also, the predicted amplitude in P3 is almost the same with the Kou and Sun model as with the numerical EMF model while it is clearly overestimated by the Tsao and Wu model. Several factors can affect the ripple amplitude. Among them are the thickness of the liquid layer beneath the ripple, and the current (or flow field) within this layer. According to Fig. 13b the thickness of the liquid layer beneath the ripple is rather uniform between P1 and P3. On the other hand the recirculation flow patterns are clearly different between P1 and P3 for the three EMF models, Fig. 9b. They could contribute to the differences in the space-evolution of the ripple amplitude obtained with the three EMF models.

6. Conclusions

The three electromagnetic force models most commonly applied to fluid dynamics simulation of melt pools formed with an electric arc were investigated. One was numerical and the two others analytical (Kou and Sun [16], and Tsao and Wu [17]). The underlying assumptions were first recalled and their impact on the computed electromagnetic force studied. These models were then applied combined with a thermo-fluid model to compare their effect on the melt pool flow, geometry and ripples from drop impact during metal transfer with a gas metal arc. From the obtained results and their analysis, the following conclusions and recommendations are drawn:

1. When an electric arc is operated in conduction mode on a workpiece with local thickness $\gtrsim$ 10 mm, it has negligible effect on the electromagnetic force acting in the melt pool area to ground the electric potential (V) at the lower surface of the workpiece rather than at the lateral ones. In these specific conditions, the analytical EMF models can therefore be applied to study a problem with V grounded at the lower surface although assumption (ix-(a)) is not satisfied, since then the electromagnetic force predicted in the melt pool is not undermined by the inappropriate grounding.
2. It should not be presumed that conclusion 1 holds also for an electric arc operated in keyhole mode. Further investigation is recommended in such case.
3. For small workpiece thickness, e.g., 4 mm, the electromagnetic force in the melt pool area is very different when changing the electric potential ground from the lower to the lateral faces. It is therefore advised to avoid using any of the analytic EMF models when the metal thickness under the arc is less than $\approx$ 10 mm and an underside electric potential ground is applied in the experiments to be simulated. The numerical EMF model (either the complete or the simplified variant) is then strongly

recommended, as it gives the freedom to set the true boundary conditions for V. It is stressed that if the arc is positioned above a groove e.g., a Y-groove, the thickness to consider is the root face height rather than the workpiece thickness.

4. The assumption of axisymmetic electromagnetic field (assumption (x)) does not imply that the contribution of the radial current density (J_r) to the azimuthal magnetic field (B_θ) is negligible in the melt pool.
5. The two analytical models and the simplified variant (based on Biot-Savart law) of the numerical EMF model do all neglect the contribution of J_r to B_θ (assumption (xi)). The complete variant of the numerical EMF model (Section 2.1) is the only one among the studied EMF models that does not neglect this contribution.
6. Neglecting the contribution of J_r to B_θ leads to an overestimation (in absolute value) of the components of the electromagnetic force in the melt pool area. In the studied GMAW problem this overestimation reached locally about 90%.
7. The simplifying assumptions (xii)–(xiii), which are specific to the Tsao and Wu model, significantly change the components of the electromagnetic force in the melt pool area compared to any of the other models. These changes are in different proportions depending on the force component as well as the distance from the free surface. The discrepancy with the other (less simplified) models locally reached more than one order of magnitude in the studied GMAW application.
8. The assumptions that fundamentally distinguish each of the studied EMF models result in the prediction of different recirculation flow patterns in the GMA melt pool while using the same closure parameters (Section 4.2), as observed in the test case of this study. In turn, they result in clear differences in the computed maximum velocity amplitude, thermal convection, melt pool morphology, bead dimensions and proportions, and free surface response to the metal transfer, depending on the EMF model selected.
9. Although the model of Kou and Sun (and the simplified variant of the numerical model) overestimates the electromagnetic force, it led to a satisfactory qualitative prediction of the flow recirculation, free surface response to drop impact, ripple propagation, and melt pool morphology compared to the more complete numerical EMF model (Section 2.1). These computational outputs were on the contrary significantly distorted with the model of Tsao and Wu in the investigated GMA problem while using the same closure parameters as with the other EMF models.
10. Above listed deficiencies of the electromagnetic forces predicted by the analytical models (and the simplified numerical model) can be compensated by tuning the amplitude of other forces applied by the arc on the melt pool to recover satisfying agreement with measured bead width and penetration depth (specifically under the arc). For instance, strategies already in use in the literature consist in adjusting the arc pressure (resp. the arc shear stress) to counterbalance the underestimation of the electromagnetic force along the vertical (resp. radial) direction by the Tsao and Wu (resp. Kou and Sun) model. Therefore, if the aim is to evaluate the effect of the different forces acting on the melt pool flow individually, this approach can be inappropriate since it can be biased by construction. Then, the complete variant of the numerical EMF model (Section 2.1) is instead strongly recommended.
11. As the assumptions specific to the analytical EMF models (and the simplified variant of the numerical EMF model) alter the predicted thermal flow compared to the more general numerical EMF model, this last one is recommended when seeking for a quantitative prediction of the melt pool. Yet, also this last one is based on assumptions (see Section 2.1) that may require further consideration in a future study.

Declaration of Competing Interest

The authors declare that they have no known competing financial interests or personal relationships that could have appeared to influence the work reported in this paper.

CRediT authorship contribution statement

P. Aryal: Methodology, Software, Validation, Investigation, Visualization, Writing – original draft. **F. Sikström:** Conceptualization, Validation, Investigation, Writing – review & editing. **H. Nilsson:** Methodology, Writing – review & editing. **I. Choquet:** Conceptualization, Methodology, Validation, Investigation, Visualization, Writing – review & editing, Supervision.

Acknowledgments

This research work is supported by grants from the EU project - Horizon 2020: INTEGRADDE, which is gratefully acknowledged. The computations were performed on resources provided by the Swedish National Infrastructure for Computing (SNIC) at NSC which is gratefully acknowledged. The authors would also like to thank Kjell Hurtig for his technical support during experiments.

Supplementary material

Supplementary material associated with this article can be found, in the online version, at doi:10.1016/j.ijheatmasstransfer.2022.123068.

References

[1] A. Murphy, M. Tanaka, K. Yamamoto, S. Tashiro, J. Lowke, K. Ostrikov, Modelling of arc welding: the importance of including the arc plasma in the computational domain, Vacuum 85 (5) (2010) 579–584.
[2] S. Cadiou, M. Courtois, M. Carin, W. Berckmans, P. Le Masson, Heat transfer, fluid flow and electromagnetic model of droplets generation and melt pool behaviour for wire arc additive manufacturing, Int. J. Heat Mass Transf. 148 (2020) 119102.
[3] X. Bai, P. Colegrove, J. Ding, X. Zhou, C. Diao, P. Bridgeman, J. roman Hönnige, H. Zhang, S. Williams, Numerical analysis of heat transfer and fluid flow in multilayer deposition of PAW–based wire and arc additive manufacturing, Int. J. Heat Mass Transf. 124 (2018) 504–516.
[4] M. Cho, Numerical simulation of arc welding process and its application, The Ohio State University, 2006 PhD Dissertation.
[5] W. Zhang, C.-H. Kim, T. DebRoy, Heat and fluid flow in complex joints during gas metal arc welding' Part II: application to fillet welding of mild steel, J. Appl. Phys. 95 (9) (2004) 5220–5229.
[6] J.-W. Na, S.-J. Kim, A study on the effect of contact tube-to-workpiece distance on weld pool shape 1n gas metal are welding, Weld. J. 74 (1995) 141s–152s.
[7] A. Murphy, Influence of droplets in gas–metal arc welding: new modelling approach, and application to welding of aluminium, Sci. Technol. Weld. Joining 18 (1) (2013) 32–37.
[8] X. Zhou, H. Zhang, G. Wang, X. Bai, Three-dimensional numerical simulation of arc and metal transport in arc welding based additive manufacturing, Int. J. Heat Mass Transf. 103 (2016) 521–537.
[9] K. Hashimoto, Y. Hirata, K. Kadota, Y. Ogino, Three-dimensional numerical model of short-circuiting transfer in GMAW, Weld. World 64 (12) (2020) 2011–2017.
[10] J. Liu, Z. Rao, S. Liao, H.-L. Tsai, Numerical investigation of weld pool behaviors and ripple formation for a moving GTA welding under pulsed currents, Int. J. Heat Mass Transf. 91 (2015) 990–1000.
[11] I. Choquet, A. Javidi Shirvan, H. Nilsson, On the choice of electromagnetic model for short high-intensity arcs, applied to welding, J. Phys. D 45 (2012) 205203.
[12] J. Hu, H. Guo, H.-L. Tsai, Weld pool dynamics and the formation of ripples in 3D gas metal arc welding, Int. J. Heat Mass Transf. 51 (9–10) (2008) 2537–2552.
[13] Y. Wang, H. Tsai, Effects of surface active elements on weld pool fluid flow and weld penetration in gas metal arc welding, Metall. Mater. Trans. B 32B (2001) 501–515.

[14] Z. Rao, J. Zhou, S. Liao, H.-L. Tsai, Three-dimensional modeling of transport phenomena and their effect on the formation of ripples in gas metal arc welding, J. Appl. Phys. 107 (5) (2010) 054905.
[15] J. Liu, Z. Rao, S. Liao, H. Tsai, Numerical investigation of weld pool behaviors and ripple formation for a moving GTA welding under pulsed currents, Int. J. Heat Mass Transf. 91 (2015) 990–1000.
[16] S. Kou, D. Sun, Fluid flow and weld penetration in stationary arc welds, Metall. Trans. A 16 (1) (1985) 203–213.
[17] K. Tsao, C. Wu, Fluid flow and heat transfer in GMA weld pools, Weld. J. 67 (3) (1988) 70s–75s.
[18] D.-W. Cho, S.-J. Na, M.-H. Cho, J.-S. Lee, Simulations of weld pool dynamics in V-groove GTA and GMA welding, Weld. World 57 (2) (2013) 223–233.
[19] L. Wu, J. Cheon, D.V. Kiran, S.-J. Na, CFD simulations of GMA welding of horizontal fillet joints based on coordinate rotation of arc models, J. Mater. Process. Technol. 231 (2016) 221–238.
[20] Z. Zhang, C. Wu, Effect of fluid flow in the weld pool on the numerical simulation accuracy of the thermal field in hybrid welding, J. Manuf. Process. 20 (2015) 215–223.
[21] H. Hamed Zargari, K. Ito, M. Kumar, A. Sharma, Visualizing the vibration effect on the tandem-pulsed gas metal arc welding in the presence of surface tension active elements, Int. J. Heat Mass Transf. 161 (2020) 120310.
[22] J. Chen, C. Schwenk, C.S. Wu, M. Rethmeier, Predicting the influence of groove angle on heat transfer and fluid flow for new gas metal arc welding processes, Int. J. Heat Mass Transf. 55 (1–3) (2012) 102–111.
[23] A. Ebrahimi, A. Babu, C.R. Kleijn, M.J. Hermans, I.M. Richardson, The effect of groove shape on molten metal flow behaviour in gas metal arc welding, Materials 14 (23) (2021) 7444.
[24] C. Zhu, J. Cheon, X. Tang, S.-J. Na, F. Lu, H. Cui, Effect of swing arc on molten pool behaviors in narrow-gap GMAW of 5083 Al–alloy, J. Mater. Process. Technol. 259 (2018) 243–258.
[25] D.-W. Cho, J.-H. Park, H.-S. Moon, A study on molten pool behavior in the one pulse one drop GMAW process using computational fluid dynamics, Int. J. Heat Mass Transf. 139 (2019) 848–859.
[26] W.-I. Cho, S.-J. Na, Impact of driving forces on molten pool in gas metal arc welding, Weld. World 65 (9) (2021) 1735–1747.
[27] D.-W. Cho, Y.-D. Park, M. Cheepu, Numerical simulation of slag movement from Marangoni flow for GMAW with computational fluid dynamics, Int. Commun. Heat Mass Transf. 125 (2021) 105243.
[28] M. Sohail, M. Karhu, S.-J. Na, S.-W. Han, V. Kujanpaa, Effect of leading and trailing torch configuration on mixing and fluid behavior of laser-gas metal arc hybrid welding, J. Laser Appl. 29 (4) (2017) 042009.
[29] D. Wu, S. Tashiro, Z. Wu, K. Nomura, X. Hua, M. Tanaka, Analysis of heat transfer and material flow in hybrid KPAW–GMAW process based on the novel three dimensional CFD simulation, Int. J. Heat Mass Transf. 147 (2020) 118921.
[30] X. Meng, G. Qin, Z. Zou, Sensitivity of driving forces on molten pool behavior and defect formation in high–speed gas tungsten arc welding, Int. J. Heat Mass Transf. 107 (2017) 1119–1128.
[31] G. Xu, J. Wang, P. Li, J. Zhu, Q. Cao, Numerical analysis of heat transfer and fluid flow in swing arc narrow gap GMA welding, J. Mater. Process. Technol. 252 (2018) 260–269.
[32] X. Chen, G. Yu, X. He, S. Li, Z. Li, Numerical study of heat transfer and solute distribution in hybrid laser–MIG welding, Int. J. Therm. Sci. 149 (2020) 106182.
[33] H. Hamed Zargari, K. Ito, M. Kumar, A. Sharma, Visualizing the vibration effect on the tandem–pulsed gas metal arc welding in the presence of surface tension active elements, Int. J. Heat Mass Transf. 161 (2020) 120310.
[34] W. Zhao, Y. Wei, J. Long, J. Chen, R. Liu, W. Ou, Modeling and simulation of heat transfer, fluid flow and geometry morphology in GMAW–based wire arc additive manufacturing, Weld. World 65 (8) (2021) 1571–1590.
[35] A. Kumar, T. DebRoy, Calculation of three-dimensional electromagnetic force field during arc welding, J. Appl. Phys. 94 (2) (2003) 1267–1277.
[36] M. Benilov, Modeling the physics of interaction of high-pressure arcs with their electrodes: advances and challenges, J Phys D 53 (2020) 013002.
[37] F. Rösler, D. Brüggemann, Shell-and-tube type latent heat thermal energy storage: numerical analysis and comparison with experiments, Heat Mass Transf. 47 (8) (2011) 1027–1033.
[38] A. Ebrahimi, C.R. Kleijn, I.M. Richardson, Sensitivity of numerical predictions to the permeability coefficient in simulations of melting and solidification using the enthalpy-porosity method, Energies 12 (22) (2019).
[39] P. Sahoo, T. Debroy, M. McNallan, Surface tension of binary metal' surface active solute systems under conditions relevant to welding metallurgy, Metall. Trans. B 19 (3) (1988) 483–491.
[40] J.U. Brackbill, D.B. Kothe, C. Zemach, A continuum method for modeling surface tension, J. Comput. Phys. 100 (1992) 335–354.
[41] M. Courtois, M. Carin, P. Le Masson, S. Gaied, M. Balabane, A complete model of keyhole and melt pool dynamics to analyze instabilities and collapse during laser welding, J. Laser Appl. 26 (4) (2014) 042001.
[42] H. Weller, Derivation, Modelling and Solution of the Conditionally Averaged Two-Phase Flow Equations, No Technical Report TR/HGW, Nabla Ltd, 2002.
[43] M. Lin, T. Eagar, Pressures produced by gas tungsten arcs, Metall. Trans. B 17 (3) (1986) 601–607.
[44] A. Haelsig, P. Mayr, Energy balance study of gas-shielded arc welding processes, Weld. World 57 (5) (2013) 727–734.
[45] N.S. Eagar, T. Tsai, Distribution of the heat and current fluxes in gas tungsten arcs, Metall. Trans. B 16B (1985) 841–846.
[46] Y.T. Cho, S.-J. Na, Application of Abel inversion in real-time calculations for circularly and elliptically symmetric radiation sources, Meas. Sci. Technol. 16 (3) (2005) 878–884.
[47] D. Wu, A. Van Nguyen, S. Tashiro, X. Hua, M. Tanaka, Elucidation of the weld pool convection and keyhole formation mechanism in the keyhole plasma arc welding, Int. J. Heat Mass Transf. 131 (2019) 920–931.
[48] A. Ebrahimi, C.R. Kleijn, I.M. Richardson, A simulation-based approach to characterise melt-pool oscillations during gas tungsten arc welding, Int. J. Heat Mass Transf. 164 (2021).
[49] C. Zhu, X. Tang, Y. He, F. Lu, H. Cui, Study on arc characteristics and their influences on weld bead geometry in narrow gap GMAW of 5083 All-alloy, Int. J. Adv. Manuf.Technol. 90 (9) (2017) 2513–2525.
[50] Q. Lin, X. Li, S. Simpson, Metal transfer measurements in gas metal arc welding, J. Phys. D 34 (3) (2001) 347–353.
[51] V. Rat, A. Pascal, J. Aubreton, M.-F. Elchinger, P. Fauchais, D. Vacher, Transport coefficients including diffusion in a two temperature argon plasma, J. Phys. D 35 (2002) 981–991.
[52] L. Barka, M. Balat-Pichelin, J.-L. Sans, E. Bêche, Oxidation and emissivity of Invar 36 alloy in air plasma at high temperatures, J. Alloys Compd. 772 (2019) 1003–1016.
[53] P.-Q. Xu, C.-M. Bao, F.-G. Lu, C.-W. Ma, J.-P. He, H.-C. Cui, S.-L. Yang, Numerical simulation of laser–tungsten inert arc deep penetration welding between WC–Co cemented carbide and Invar alloys, Int. J. Adv. Manuf.Technol. 53 (9) (2011) 1049–1062.
[54] A. Seifter, K. Boboridis, B. Didoukh, G. Pottlacher, P. Jäger, Thermophysical properties of liquid Fe64/Ni36 (invar®), J. Chimie Phys. 94 (1997) 1004–1008.
[55] K.C. Mills, Recommended Values of Thermophysical Properties for Selected Commercial Alloys, Woodhead Publishing, 2002.
[56] X. Zhan, X. Liu, Y. Wei, W. Ou, J. Chen, H. Liu, Numerical simulation on backward deformation of mig multi-layer and multi-pass welding of thick Invar alloy, Int. J. Adv. Manuf. Technol. 92 (1) (2017) 1001–1012.
[57] J. Brillo, I. Egry, Surface tension of nickel, copper, iron and their binary alloys, J. Mater. Sci. 40 (9) (2005) 2213–2216.
[58] J.R. Rumble, et al., CRC Handbook of Chemistry and Physics, vol. 100, CRC Press Boca Raton, 2018, p. 1309.
[59] Y. Çengel, Heat and Mass Transfer: A Practical Approach (SI Units), 3rd ed., McGraw Hill, 2007.
[60] A. Kidess, S. Kenjereš, C.R. Kleijn, The influence of surfactants on thermocapillary flow instabilities in low Prandtl melting pools, Phys. Fluids 28 (6) (2016).
[61] Z. Hu, L. Hua, X. Qin, M. Ni, F. Ji, M. Wu, Molten pool behaviors and forming appearance of robotic GMAW on complex surface with various welding positions, J. Manuf. Process. 64 (2021) 1359–1376.
[62] K. Park, H. Jeong, S. Baek, D.-Y. Kim, M.-J. Kang, J. Cho, Turbulent molten pool analysis of tandem GMA automotive steel sheet welding, Int. J. Heat Mass Transf. 129 (2019) 1–6.
[63] A. Ebrahimi, C. Kleijn, I. Richardson, Numerical study of molten metal melt pool behaviour during conduction-mode laser spot melting, J. Phys. D 54 (2021) 105304.